Title

Multi-scale, open-system magmatic and sub-solidus processes contribute to the chemical and isotopic characteristics of the Jurassic Guadalupe Igneous Complex, Sierra Nevada, California, USA

Authors

Ratschbacher, Barbara C

Ardill, Katie

Keller, C Brenhin

et al.

Publication Date

2024-05-17

DOI

10.1130/ges02689.1

Peer reviewed

Research Paper

THEMED ISSUE: Different Personalities of Granites and Rhyolites: Silicic Magmas from the Lower Crust to the Surface

GEOSPHERE

GEOSPHERE

https://doi.org/10.1130/GES02689.1

12 figures; 2 tables; 2 sets of supplemental files

CORRESPONDENCE:
barbara.ratschbacher@gmail.com

CITATION: Ratschbacher, B.C., Ardill, K., Keller, C.B., Schoene, B., Paterson, S.R., Putirka, K.D., Lackey, J.S., and Paige, M.L., 2024, Multi-scale, open-system magmatic and sub-solidus processes contribute to the chemical and isotopic characteristics of the Jurassic Guadalupe Igneous Complex, Sierra Nevada, California, USA: Geosphere, https://doi.org/10.1130/GES02689.1.

Science Editor: Shanaka de Silva
Guest Associate Editor: Jonathan S. Miller

Received 12 June 2023
Revision received 1 January 2024
Accepted 17 February 2024

Published online 17 May 2024

Multi-scale, open-system magmatic and sub-solidus processes contribute to the chemical and isotopic characteristics of the Jurassic Guadalupe Igneous Complex, Sierra Nevada, California, USA

Barbara C. Ratschbacher[1], Katie Ardill[2], C. Brenhin Keller[3], Blair Schoene[4], Scott R. Paterson[5], Keith D. Putirka[6], Jade Star Lackey[7], and Matthew L. Paige[8]

[1]Department of Earth and Planetary Sciences, University of California Davis, Davis, California 95616, USA
[2]Department of Geosciences, Texas Tech University, Lubbock, Texas 79409, USA
[3]Department of Earth Sciences, Dartmouth College, Hanover, New Hampshire 03755, USA
[4]Department of Geosciences, Princeton University, Princeton, New Jersey 08544, USA
[5]Retired, Claremont, California 91711, USA
[6]Department of Earth and Environmental Sciences, California State University Fresno, Fresno, California 93720, USA
[7]Geology Department, Pomona College, Claremont, California 91711, USA
[8]Owens Corning Science and Technology Center, Granville, Ohio 43023, USA

ABSTRACT

The chemical and isotopic characteristics of a solidified pluton represent the integration of magmatic and sub-solidus processes operating across a range of spatial and temporal scales during pluton construction, crystallization, and cooling. Disentangling these processes and understanding where chemical and isotopic signatures were acquired requires the combination of multiple tools tracing processes at different time and length scales. We combine whole-rock oxygen and Sr-Nd isotopes, zircon oxygen isotopes and trace elements, and mineral compositions with published high-precision U-Pb zircon geochronology to evaluate differentiation within the bimodal Guadalupe Igneous Complex, Sierra Nevada, California (USA). The complex was constructed in ~300 k.y. between 149 and 150 Ma. Felsic magmas crystallized as centimeter- to meter-sized segregations in gabbros in the lower part of the complex and as granites and granophyres structurally above the gabbros. A central mingling zone separates the mafic and felsic units. Pluton-wide $\delta^{18}O_{(whole\text{-}rock)}$, $\delta^{18}O_{(zircon)}$, and Sr-Nd isotopic ranges are too large to be explained by in situ, closed-system differentiation, instead requiring open-system behavior at all scales. Low $\delta^{18}O_{(whole\text{-}rock)}$ and $\delta^{18}O_{(zircon)}$ values indicate assimilation of hydrothermally altered marine host rocks during ascent and/or emplacement. In situ differentiation processes operated on a smaller scale (meters to tens of meters) for at least ~200 k.y. via (1) percolation and segregation of chemically and isotopically diverse silicic interstitial melt from a heterogeneous gabbro mush; (2) crystal accumulation; and (3) sub-solidus, high-temperature, hydrothermal alteration at the shallow roof of the complex to modify the chemical and isotopic characteristics. Whole-rock and mineral chemistry in combination with geochronology allows deciphering open-system differentiation processes at the outcrop to pluton scale from magmatic to sub-solidus temperatures over time scales of hundreds of thousands to millions of years.

Barbara Ratschbacher https://orcid.org/0000-0002-2112-7225

1. INTRODUCTION

Disentangling the processes that create the chemical and isotopic characteristics of plutonic complexes (e.g., fractional crystallization, magma mixing, assimilation, sub-solidus alteration) and investigating the extent that these processes take place at the emplacement level is important for understanding continental crust formation and the volcanic-plutonic connection (e.g., Ducea et al., 2015; Bachmann and Huber, 2016). Sustained elevated temperatures supplied by basaltic, mantle-derived melts to the lower crust support the formation of lower-crustal MASH zones (i.e., zones of intensive melting, assimilation, storage, and homogenization: Hildreth and Moorbath, 1988; or deep crustal hot zones: Annen et al., 2006) as primary magma storage and differentiation sites in arcs. However, recent geophysical, petrological, and numerical modeling studies indicate that magma storage and differentiation can occur throughout the arc crust (e.g., Cashman et al., 2017; Delph et al., 2021; Barnes et al., 2021; Hildreth, 2021). Considerable debate still exists as to the extent to which differentiation processes may operate in the shallow crust (e.g., Bachmann and Huber, 2016). Cold ambient temperatures and the rarity of mafic cumulates in the shallow crust of many arcs argue against extensive differentiation in the upper crust (e.g., Keller et al., 2015). Still, large-volume eruptions equilibrated at upper-crustal pressures attest to the presence of large upper-crustal magma reservoirs (e.g., Bachmann and Huber, 2016).

Solidified shallow-crustal plutons provide opportunities for studying the extent of differentiation and magma–host rock interaction in the upper crust. These plutons reflect the time-integrated record of multiple magmatic and sub-solidus events that generate compositionally and isotopically diverse intrusive complexes. Plutonic bodies may be constructed incrementally with multiple recharging events and experience remelting ("defrosting") of solidified units, magma mixing, fractional crystallization, and assimilation or recycling at multiple scales during their active magmatic lifespan as well as sub-solidus

alteration after solidification (e.g., Harper et al., 2004; Bindeman et al., 2008; Coint et al., 2013; Barth et al., 2016; Barnes and Werts, 2022). Geochemical tools such as radiogenic and stable isotope analysis, mineral and whole-rock chemistry, and numerical modeling are used to unravel these processes (e.g., Wotzlaw et al., 2012; Fiedrich et al., 2017; Barnes et al., 2021; Payacán et al., 2023). Each tool tracks different processes at different scales; for example, zircon geochemistry records the melt composition at zircon saturation and crystallization, which can occur early or late with respect to the crystallization of other mineral phases either in the source region of a magma or at the emplacement level (e.g., Broderick et al., 2015; Samperton et al., 2015). Whole-rock geochemistry, on the other hand, integrates across a wide range of mineral compositions and thus may or may not reflect liquid compositions (Barnes et al., 2019; Cornet et al., 2022). A combination of various geochemical tools, recording the evolution of an intrusive complex at different time and length scales, allows disentanglement of the contributions of multiple processes to the observed chemical and isotopic diversity.

In this study, we combine new whole-rock and mineral isotope compositions and major and trace element mineral geochemistry to investigate the magmatic and sub-solidus processes affecting the Late Jurassic Guadalupe Igneous Complex (GIC) in the Sierra Nevada, California, USA. The GIC is a tilted, shallow-crustal, and compositionally bimodal (gabbro and granite) pluton emplaced in marine metasedimentary host rocks of similar age (Best, 1963; Haeussler and Paterson, 1993; Putirka et al., 2014). Previous work using high-precision U-Pb zircon isotope dilution thermal ionization mass spectrometry (ID-TIMS) geochronology has demonstrated that mafic and felsic magmas are coeval in the GIC (Ratschbacher et al., 2018) and syn-magmatic deformation occurred in the Bear Mountains fault zone (BMFZ) at the exposed base of the pluton (Paterson et al., 1987; Saleeby et al., 1989; Vernon et al., 1989). We aim to understand how much of the chemical and isotopic characteristics in the GIC can be attributed to (1) processes in the deeper, unexposed parts of the magmatic system; (2) in situ differentiation at the emplacement level; or (3) sub-solidus processes affecting the pluton after solidification. By combining geochemical tools capable of tracing magmatic processes on various time and length scales, we show that the chemical and isotopic characteristics of the GIC require initial magmatic differentiation below the emplacement level, during ascent, and at the emplacement level.

2. GEOLOGIC SETTING

The GIC, located in the western foothills of the Sierra Nevada, California (Fig. 1), is one of several Jurassic arc plutons emplaced into fault-bounded, Triassic–Jurassic accreted terranes of metavolcanic and metasedimentary rocks, which collectively form the Western Metamorphic Belt (e.g., Clark, 1964; Kistler and Peterman, 1973; Tobisch et al., 1989; Snow and Scherer, 2006). The Foothills terrane, in which the GIC is located, forms the westernmost terrane of the Western Metamorphic Belt. It is bound by the Melones fault zone in the east and overlain by the Great Valley Sequence in the west (Fig. 1). The GIC intrudes metavolcanic and metasedimentary formations of oceanic affinity as well as ophiolite slivers, which experienced prehnite-pumpellyite-facies regional metamorphism (e.g., Clark, 1964; Tobisch et al., 1989; Paterson et al., 1991; Saleeby et al., 1992; Snow and Scherer, 2006). At the top of the GIC, fine-grained rhyolites are exposed (unnamed rhyolite unit in Mariposa Formation; Schweickert, 2015, unit Jmv), which yield U-Pb zircon ID-TIMS ages ~3–4 m.y. older than the GIC (Ratschbacher et al., 2018; orange unit in Figs. 1 and 2) and thus are not part of the GIC magmatic system. The GIC intrudes the Late Jurassic marine Mariposa Formation (called the Salt Spring Slate west of the BMFZ) consisting dominantly of slate and greywacke (e.g., Clark, 1964; Paterson et al., 1987; Ernst et al., 2009). The Mariposa Formation overlies the Jurassic–Triassic volcano-sedimentary Peñon Blanco Formation, which is exposed to the north of the GIC (e.g., Bogen, 1984), and the Late Jurassic Gopher Ridge island-arc volcanics exposed to the west (Clark, 1964; Tobisch et al., 1989; Schweickert, 2015). The Jurassic arc during the time of formation of the GIC is interpreted as a fringing oceanic arc built on slightly older dominantly marine sedimentary and volcanic units and local ophiolites (Schweickert and Cowan, 1975; Attia et al., 2021). The exposed base of the GIC intersects with the BMFZ, a zone of Middle Jurassic to Early Cretaceous multi-stage ductile deformation and metamorphism (Fig. 1; Paterson et al., 1987; Saleeby et al., 1989; Miller and Paterson, 1991). Metamorphic grades as high as upper amphibolite facies in the BMFZ led to partial melting (Vernon et al., 1989; Paterson et al., 1991; Lafrance and Vernon, 1993). BMFZ activity was synchronous with magmatism in the GIC and the contemporaneous Hornitos pluton to the north of the GIC (Fig. 1), indicated by outcrop-scale magmatic to solid-state transitions, sub-magmatic to high-temperature microstructures (Vernon et al., 1989; Tobisch et al., 1991), and a U-Pb TIMS multi-grain zircon age (151 ± 1 Ma; Fig. 2; Saleeby et al., 1989) of a migmatite in the BMFZ (Fig. 3A).

2.1. Previous Work on the Guadalupe Igneous Complex

2.1.1. Petrogenetic Model of the Guadalupe Igneous Complex

Best (1963), Best and Mercy (1967), and Putirka et al. (2014) showed that the GIC is compositionally bimodal and stratified, composed of fine- to medium-grained and partly layered gabbros (49–55 wt% SiO_2; Putirka et al., 2014) at the exposed base of the complex (Fig. 2). The gabbro unit grades into a compositionally heterogenous meladiorite unit (55–75 wt% SiO_2) and fine-grained granites to granophyres (67–78 wt% SiO_2; Putirka et al., 2014) at the exposed top of the complex (Fig. 2). A mingling zone separates the dominantly mafic lower part (gabbro and meladiorite units) from the upper felsic part (granites and granophyres; Fig. 2), in which mafic and felsic magmas show limited mixing (e.g., Putirka et al., 2014; "agmatite" zone of Best, 1963). Structural and paleomagnetic studies indicate an ~28° SW-side-up tilting of the GIC, exposing an ~7-km-thick plutonic section from ~10 km intrusion depth at the base to

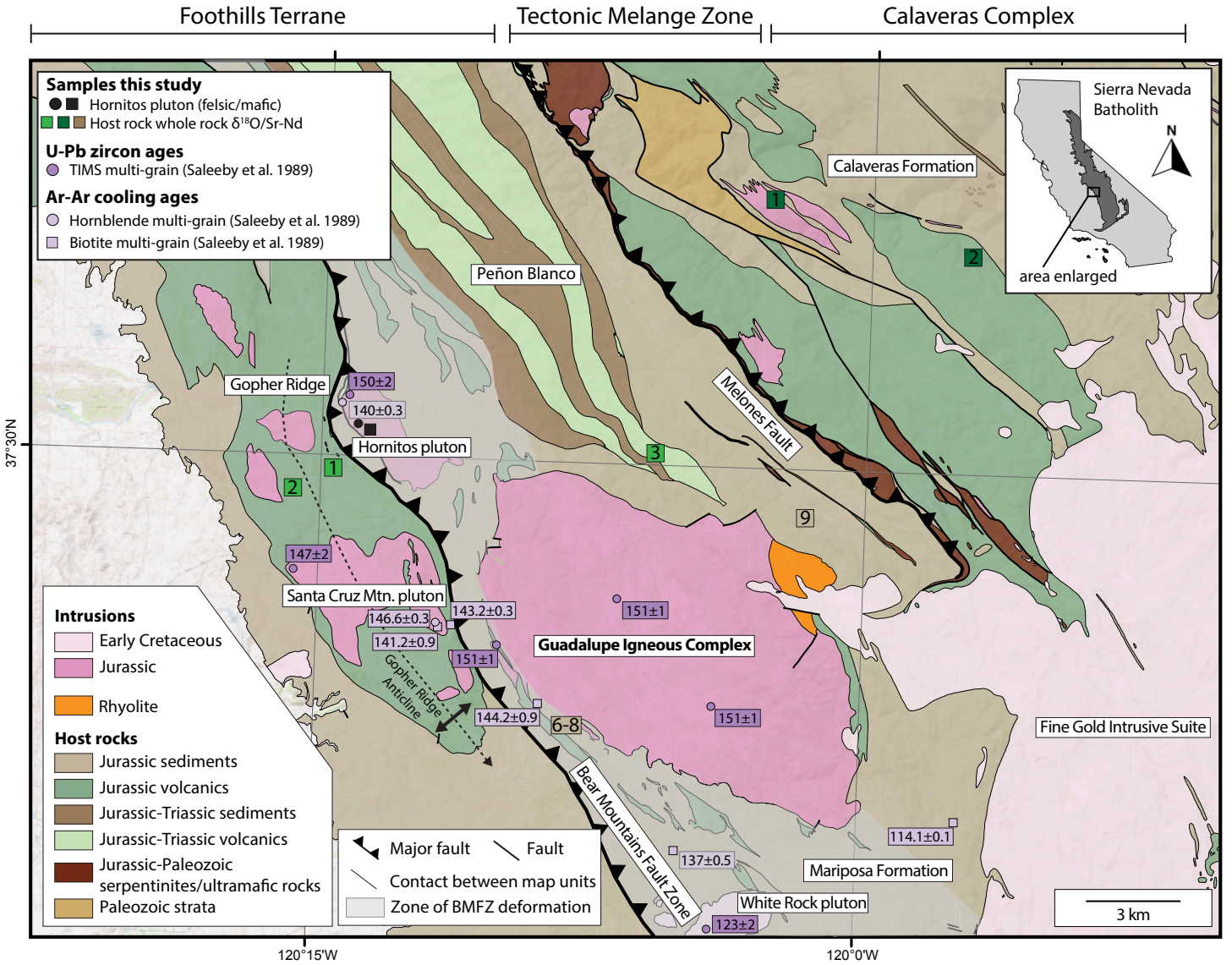

Figure 1. Geologic map of the Guadalupe Igneous Complex, California, USA, and surrounding host rocks (modified after Wills et al., 2022a, 2022b). Locations of geochronology samples from Saleeby et al. (1989) are shown with purple symbols (labeled with age in Ma). Locations of host rock samples are shown as green and brown squares; numbers in squares correspond to numbers in squares in Figure 6. Small inset depicts the location of the geologic map in context of the Sierra Nevada batholith. TIMS—thermal ionization mass spectrometry; BMFZ—Bear Mountains fault zone.

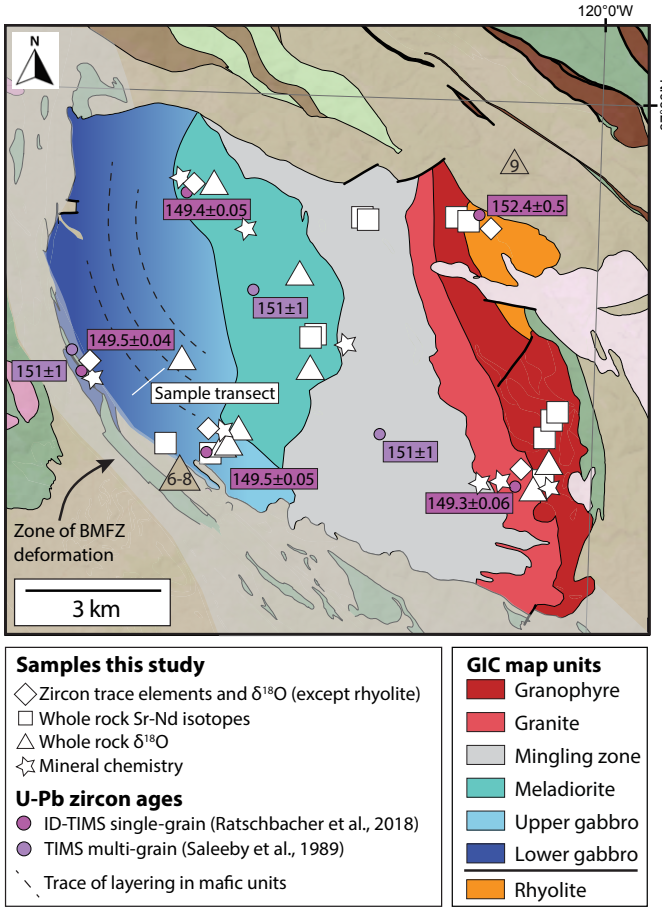

Figure 2. Map of the Guadalupe Igneous Complex (GIC) showing map units and locations of samples analyzed in this study and published geochronology samples (labeled in Ma) from Saleeby et al. (1989) and Ratschbacher et al. (2018). "Sample transect" refers to a transect of whole-rock samples collected through the lower into the upper gabbro units. ID-TIMS—(isotope dilution) thermal ionization mass spectrometry. Numbers in brown triangles correspond to numbers in triangles in Figure 8. BMFZ—Bear Mountains fault zone.

near-surface levels (Paterson et al., 1991; Haeussler and Paterson, 1993). Best and Mercy (1967) and Putirka et al. (2014) proposed an in situ differentiation model for the formation of the GIC. Using whole-rock compositional data, Putirka et al. (2014) presented a petrogenetic model involving crystal-liquid separation and mixing of differentiates. Repeated intrusion of hydrous basaltic parental magma formed the lower part of the complex, which differentiated along multiple fractionation paths to generate intermediate compositions via continuous crystal-liquid fractionation. Intermediate melts further fractionated by a discontinuous process to form mafic residues and highly evolved liquids. Local examples of such processes are felsic segregations, abundant in the upper gabbro and meladiorite units. These centimeter- to meter-sized, high-silica (68–75 wt% SiO_2; Putirka et al., 2014; Fig. 3) pods and segregations were interpreted as locally collected interstitial melt pooled from the surrounding gabbro mush (Putirka et al., 2014; Ratschbacher et al., 2018; see field description in section 4.1). Felsic differentiates were added to a growing felsic cap and mixed with underlying intermediate magmas to generate the observed compositional range in the granite and granophyre units. In situ differentiation halted when the mafic input ended.

2.1.2. Crystallization Ages of the Guadalupe Igneous Complex

Saleeby et al. (1989) obtained the first (bulk) zircon U-Pb ages of the GIC using the TIMS method (Fig. 1), showing that the mafic and felsic rocks have overlapping ages at 150–151 Ma. A 153 ± 2 Ma sensitive high-resolution ion microprobe (SHRIMP) zircon U-Pb age by Ernst et al. (2009) supported this result. Ratschbacher et al. (2018) presented the first high-precision chemical abrasion ID-TIMS zircon U-Pb ages, which constrained the crystallization ages of the mafic and felsic rocks between 149 and 150 Ma (Fig. 2). Calculated maximum zircon crystallization temperatures start at ~870 °C for both the mafic and felsic samples and last to temperatures of ~750 °C for the mafic and ~660 °C for the felsic rocks (see Ratschbacher et al., 2018, for details on calculations). The overall construction duration of the GIC was estimated at 295 ± 110 k.y. Two-dimensional finite-difference thermal modeling indicates that melt was present for ~200 k.y. after emplacement, resulting in total melt-present time scales of ~550 k.y. (Ratschbacher et al., 2018). Ratschbacher et al. (2018) further showed that zircons in one sample from a felsic segregation have the same ages, within uncertainty, as the zircons in the surrounding gabbro.

2.1.3. Cooling Ages in the Vicinity of the Guadalupe Igneous Complex

Saleeby et al. (1989) published seven $^{40}Ar/^{39}Ar$ biotite and hornblende cooling ages from plutons in the vicinity of the GIC, pluton aureoles, and host rocks within or near the BMFZ (Fig. 1). Ages from plutonic rocks yield 141.2 ± 0.9 Ma (biotite) and 146.6 ± 0.3 Ma (hornblende; both Santa Cruz Mountain pluton) and 140 ± 0.3 Ma (hornblende, Hornitos pluton; Fig. 1), and they are interpreted to represent cooling of these intrusive suites. Biotite $^{40}Ar/^{39}Ar$ ages of deformed host rocks were interpreted as metamorphic cooling ages and range from 144.2 ± 0.9 to 137 ± 0.5 Ma within the BMFZ (Fig. 1), suggesting that ductile deformation and metamorphism persisted until at least 137 Ma (Saleeby et al., 1989). One 114.1 ± 0.1 Ma age from a host rock outside the BMFZ and within the aureole of the adjacent Cretaceous Fine Gold Intrusive

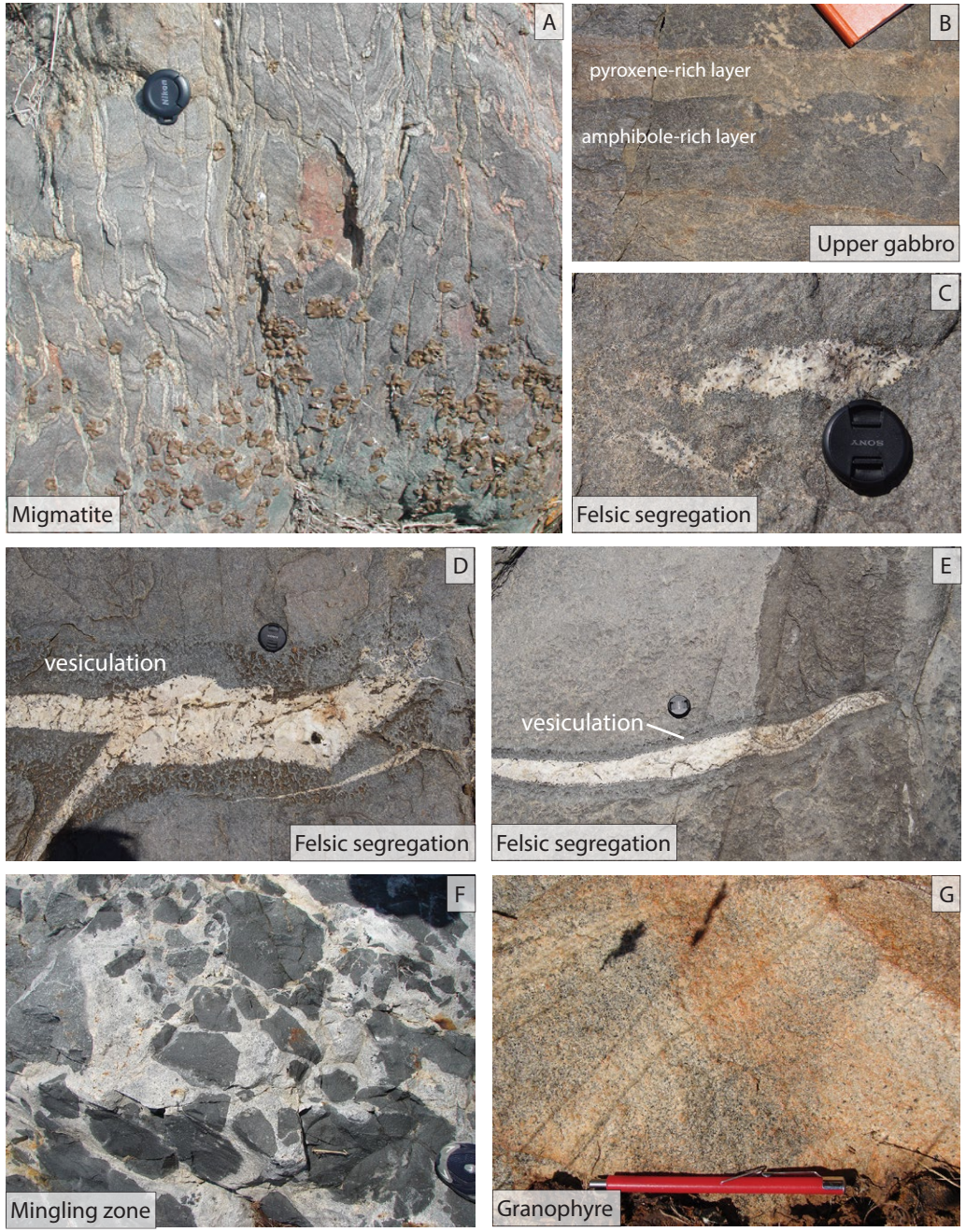

Figure 3. Field photos from the Guadalupe Igneous Complex. (A) Partial melting of Mariposa Formation in the Bear Mountains fault zone (photo first published in Vernon and Paterson, 2001). (B) Compositional layering in the upper gabbro unit. A5 field notebook for scale. (C–E) Felsic segregations in the upper gabbro unit. Note vesicular texture surrounding larger segregations (D and E), gradational boundaries in smaller segregations (C), and large grain size compared to surrounding gabbro. (F) Mingling of felsic and mafic magmas in the mingling zone (note tip of shoe for scale in lower right corner). (G) Red-stained alteration surface of granophyre outcrop.

Suite (biotite; Bass Lake Tonalite; Fig. 1) reflects cooling of this intrusive suite. One multi-grain zircon U-Pb TIMS age of 123 ± 2 Ma from the undeformed White Rock pluton provides a minimum deformation age for the BMFZ (Fig. 1).

3. METHODS

Detailed descriptions of analytical procedures for whole-rock Sr-Nd isotope analyses, whole-rock oxygen and major element geochemistry, and zircon geochemistry are in Text S1 in the Supplemental Material.[1] Brief summaries of these analytical methods are given below. Figures 1 and 2 show the locations of analyzed samples (white symbols are GIC samples; black, green, and brown samples are host rock samples).

3.1. Whole-Rock Sr-Nd isotopes

Twenty-two (22) whole-rock samples were analyzed for Sr and Nd isotopes using a VG Sector multi-collector instrument at the University of Arizona (Tucson, Arizona, USA) following the analytical protocol detailed in Otamendi et al. (2009). The estimated standard errors for the samples analyzed are $^{87}Sr/^{86}Sr$ = 0.000006–0.000019 and $^{143}Nd/^{144}Nd$ = 0.000005–0.000011. Table S1 (see footnote 1) lists the data, and Text S1 describes the analytical protocol.

3.2. Whole-Rock Oxygen Isotopes and Major and Trace Element Geochemistry

Twenty-nine (29) samples from the GIC were analyzed for whole-rock $\delta^{18}O$ values: 18 from the lower gabbro unit (Shultz Mountain area; "sample transect" in Fig. 2), five from the upper gabbro unit, one from a felsic segregation at the contact of the upper gabbro and meladiorite unit, three from the meladiorite unit, and two from the granophyre unit (Fig. 2). Additionally, we analyzed one slate from the Mariposa Formation north of the GIC and three strongly deformed gneissic Mariposa Formation samples from the exposed base of the GIC within the BMFZ (Figs. 1 and 2). Whole-rock oxygen isotope analyses were carried out at Indiana University (Bloomington, Indiana, USA) using Finnigan Delta-E and Finnigan MAT 252 mass spectrometers. Results for whole-rock oxygen isotope analyses are reported in the delta (δ) notation relative to Vienna standard mean ocean water (VSMOW; Baertschi, 1976). Analytical precision is better than 0.06‰ (2σ). Table S2 (see footnote 1) lists the $\delta^{18}O$ values in parts per mil VSMOW. Whole-rock major and selected trace elements were measured for the same samples by solution inductively coupled plasma source emission spectroscopy using a Jarrall Ash Atom Comp II at Indiana University and by instrumental neutron activation analysis (INAA) at the Phoenix Memorial Laboratory at the University of Michigan (Ann Arbor, Michigan, USA) following the procedures described in Webster and Wintsch (1987). Table S2 lists the data.

3.3. Electron Microprobe Analyses

Major and minor element abundances of pyroxene, amphibole, feldspar, and titanite were analyzed using an electron microprobe at the University of California, Los Angeles (UCLA) and the U.S. Geological Survey (USGS) Menlo Park (California). Analysis conditions at UCLA and USGS have been documented in Ratschbacher et al. (2018). Table S3 (see footnote 1) lists the data.

3.4. LA-ICP-MS Zircon Geochemistry

Zircon trace-element compositions were analyzed with a laser ablation–inductively coupled plasma mass spectrometer (LA-ICP-MS) at the University of California, Santa Barbara (UCSB), following the protocol described in Kylander-Clark et al. (2013). Figure S1 (see footnote 1) shows the location of each laser spot on cathodoluminescence (CL) images of polished zircon grains. Additionally, surfaces of unpolished zircon grains from the lower and upper gabbro units have been analyzed. Text S1 describes analytical protocols and standards, and Table S4 lists results including 2σ uncertainties.

3.5. Oxygen Isotopes in Zircon

A total of 28 in situ zircon oxygen isotope analyses were performed on 23 individual grains from five samples (Fig. 2). Oxygen isotope analyses in zircon were performed at UCLA using a CAMECA IMS 1270 in multi-collection mode with a cesium cation primary beam with a spot size of 20–25 µm and a beam current of ~15 nA, following the protocol of Trail et al. (2007). Zircons were coated with gold, and raw $^{18}O/^{16}O$ values were corrected using zircon standard AS3 ($\delta^{18}O$ = 5.34‰; Trail et al., 2007), which yielded an in-run reproducibility of 0.48‰ at the 2σ level. Values of $\delta^{18}O$ are reported in the delta (δ) notation relative to Vienna standard mean ocean water (VSMOW; Baertschi, 1976) and are listed in Table S5 (see footnote 1).

[1]Supplemental Material. Figure S1: Cathodoluminescence images of zircon grains showing spots analyzed with LA-ICP-MS. Figure S2: Comparison of Mg# in whole rock with Mg# in clinopyroxene and orthopyroxene, amphibole Si versus Mg#, and ranges in anorthite content in plagioclase from samples of various GIC map units. Figure S3: Differences in maximum Hf and Yb/Dy ratio in individual zircon grains from different map units of the GIC and as a function of zonation type. Figure S4: Assimilation-fractional crystallization and mixing calculations. Table S1: Whole-rock Sr and Nd isotope composition and major element composition. Table S2: Whole-rock oxygen isotope composition and major and selected trace element composition. Table S3: Electron microprobe data from clinopyroxene, orthopyroxene, amphibole, feldspar, and titanite. Table S4: Zircon trace element compositions. Table S5: Zircon oxygen isotopes. Table S6: Uncertainties of thermometers used in this study. Text S1: Detailed description of analytical methods and detailed description of thin section observations. Folder S1: Results of zircon trace element modeling. Please visit https://doi.org/10.1130/GEOS.S.25444633 to access the supplemental material, and contact editing@geosociety.org with any questions.

3.6. Mineral Chemometry

Early-crystallizing mineral–whole-rock equilibrium tests and mineral-melt chemometric calculations were applied to mineral analyses to test whether whole-rock compositions represent frozen melts or whether they represent cumulates that have lost melt (e.g., Barnes et al., 2016; Barnes and Werts, 2022; Cornet et al., 2022). The Fe-Mg exchange coefficient [$^{Fe/Mg}K_D = (Fe/Mg)_{mineral}/(Fe/Mg)_{rock}$] between clinopyroxene and host rocks in equilibrium is 0.28 ± 0.08, and $^{Fe/Mg}K_D$ = 0.29 ± 0.06 between orthopyroxene and host rocks (Putirka, 2008). The anorthite-albite (An-Ab) equilibrium test of Putirka (2008) was similarly applied to plagioclase (pl) analyses ($^{An-Ab}K_D = X^{pl}_{Ab}X^{rock}_{AlO_{1.5}}X^{rock}_{CaO} / X^{pl}_{An}X^{rock}_{NaO_{0.5}}X^{rock}_{SiO_2}$; mineral and liquids components, X, are calculated as cation fractions). An $^{An-Ab}K_D$ value of 0.1 ± 0.05 indicates equilibrium conditions at temperatures <1050 °C, and an $^{An-Ab}K_D$ value of 0.27 ± 0.11 is suitable for temperatures >1050 °C.

Chemometric approaches leverage experimental data sets to quantify the dependence of a mineral composition on the temperature (± pressure) and composition of the melt it crystallized from (e.g., Ridolfi and Renzulli, 2012; Putirka, 2016; Zhang et al., 2017; Scruggs and Putirka, 2018). Higgins et al. (2022) used machine learning techniques to calibrate these relationships for arc magmas in the Lesser Antilles and predict the pressure, temperature, and anhydrous melt composition (SiO_2, Al_2O_3, CaO, Na_2O, K_2O, MgO, FeO, TiO_2) for a given clinopyroxene or amphibole analysis. Standard error estimate values for the amphibole and clinopyroxene equilibrium melt models range from 0.2 to 4.7 wt% (element and mineral dependent; see Higgins et al., 2022). The equations 2 and 3 of Scruggs and Putirka (2018) were applied to plagioclase analyses to calculate equilibrium melt SiO_2 and CaO contents. SiO_2 and CaO are estimated to ±3.9 wt% and ±1.2 wt%, respectively (Scruggs and Putirka, 2018).

3.7. Thermometry

We use multiple mineral thermometers to constrain crystallization temperatures of mafic and felsic rocks in the GIC. Application of mineral thermometers may rely on (1) knowledge of the melt composition in equilibrium with the mineral composition (e.g., clinopyroxene-liquid thermometer [Putirka et al., 2003]; plagioclase-liquid thermometer [Putirka, 2005]). A melt composition could be either a whole-rock, glass, melt inclusion, or a calculated equilibrium melt composition; (2) pressure (e.g., Putirka, 2016, equation 6); or (3) mineral compositions alone (e.g., Putirka, 2016, equation 5; Higgins et al., 2022). Where thermometers required a melt input, the whole-rock composition was used only if it passed the mineral-whole rock equilibrium tests described in the previous section. Given the low number of analyses that fulfill this requirement (see section 4), the calculated equilibrium melt composition was used if available (e.g., clinopyroxene and amphibole; Higgins et al., 2022). The following thermometers were applied to the data set:

- *Clinopyroxene (cpx):* Higgins et al. (2022) (cpx-only); Putirka et al. (1996, 2003) (cpx-liquid; whole-rock composition was used as a liquid composition if in equilibrium with cpx; valid for only one gabbro from the upper gabbro unit);
- *Orthopyroxene (opx):* Kohler and Brey (1990) (opx-only; assuming a pressure of 2 kbar);
- *Plagioclase (pl):* Putirka (2005, equation 2; pl-liquid; whole-rock composition was used as a liquid composition if in equilibrium with pl; water contents of 3.5 wt% in the lower and upper gabbro and 4 wt% in the mingling zone and granophyre units); rhyolite-MELTS (Gualda et al., 2012) modelling was used to determine the onset of plagioclase crystallization in each unit; the lowest-SiO_2 equilibrium melt calculated from pyroxene and amphibole compositions (Higgins et al., 2022) was used as the starting melt composition;
- *Amphibole (amp):* Putirka (2016, equation 5; amp-only; pressure-independent); Higgins et al. (2022; amp-only);
- *Titanite (ttn):* Hayden et al. (2008, equation 7; ttn-only; activities of TiO_2 and SiO_2 of 1);
- *Zircon (zrn):* Ferry and Watson (2007, equation 15; zrn-only; TiO_2 activity of 0.5 (presence of ilmenite), and SiO_2 activity of 1 for quartz-bearing and 0.8 for quartz-free samples; zrn crystallization temperatures were also estimated by calculating zircon saturation distributions; see Ratschbacher et al., 2018, for details).

4. RESULTS

4.1. Field Observations

Varying mineral proportions define modal layering in the gabbro, commonly by the presence or absence of amphibole and/or varying grain size. Compositional layering is more pronounced in the lower gabbro than the upper gabbro, but monomineralic rocks rarely occur. Subtle layering between amphibole- and pyroxene-dominated gabbro occurs in the upper gabbro (Fig. 3B). Igneous layering dips to the east, and dip magnitude ranges from sub-vertical dips to 40° (Best, 1963) toward the top of the complex. Numerous centimeter- to meter-sized felsic segregations occur in the upper gabbro, exhibiting elongated tear shapes with high aspect ratios (usually >5:1; Figs. 3C–3E). On average, their long axes point to the top of the complex, commonly at a high angle to the sub-vertical layering in the gabbros. The contact between the felsic segregation and the surrounding gabbro is gradational in small segregations (Fig. 3C) but sharp in large ones and characterized by vesiculation (Figs. 3D and 3E). The tips of segregations are round and/or irregular (Fig. 3C and 3E). The segregations have a larger grain size (as large as several centimeters) than the surrounding gabbros and abundant hydrous mineral phases (amphibole, biotite). The meladiorite unit is compositionally heterogenous (gabbro to granite), but limited exposure does not allow the estimation of proportions of mafic and felsic domains. Like in the upper gabbro unit, felsic segregations occur, but they tend to be larger in size (as large as multiple tens of meters). The mingling zone

separating dominantly mafic and felsic units shows evidence for mutual intrusions of mafic and felsic magmas. Field observations indicate emplacement of sub-parallel gabbroic dikes into granitic hosts (Putirka et al., 2014, their figure 8A) and net veining of felsic magma breaking up mafic blocks (Fig. 3F). This indicates that both felsic and mafic magmas were present during the formation of the mingling zone. Although exposure is limited, a gradual disappearance of mafic dikes and enclaves marks the transition into the felsic units (granite and granophyre) at the top of the GIC. The felsic units were pervasively altered in parts as evidenced by red staining on surfaces and along fractures (Fig. 3G).

4.2. Mineralogy and Textures

Petrographic descriptions are based on thin section observations of samples collected in this study and observations from Best (1963), Best and Mercy (1967), Putirka et al. (2014), and Canchola (2016). Petrographic observations from each unit are summarized in Table 1 and described in detail in Text S1 (see footnote 1). Representative thin section images are shown in Figure 4.

4.3. Zircon Textures

Six samples were collected for textural investigations and geochemistry of zircon (Fig. 2): (1) amphibole (meta)hornblendite (sample BRGIC13) from the lower gabbro unit within the BMFZ; (2) amphibole-pyroxene gabbro (BRGIC10) from the upper gabbro unit, which was collected ~1 m away from (3) felsic segregation sample 10D, collected from the upper gabbro unit; (4) pyroxene gabbro (BRGIC3) from the meladiorite unit; (5) granite (BRGIC2) from the granite unit; and (6) a rhyolite (BRGIC5; no zircon oxygen isotope data). These samples are described in detail in Ratschbacher et al. (2018) and have been dated with zircon U-Pb CA-ID-TIMS geochronology. Zircon textures in the six investigated samples are simple, lacking obvious inherited cores and showing either no zoning or one zoning type (Fig. S1 [see footnote 1]). The cathodoluminescence (CL) images show concentric, sector, and patchy zonation, defined as follows: (1) Concentric zoning exhibits repeated, oscillatory and parallel zones of various thicknesses; (2) sector zoning shows bright and dark zones separated by straight boundaries; and (3) patchy zoning has irregularly shaped and chaotic bright and dark domains, which do not show a repeated pattern.

4.4. Mineral Chemistry

4.4.1. Clinopyroxene

Mg# [molar Mg/(Mg + Fe_{total})] of clinopyroxene ranges from 0.54 to 0.80 and is higher in amphibole gabbros (0.73–0.80; $n = 3$) and lower in pyroxene-gabbros (0.54–0.65; $n = 2$; Fig. S2 [see footnote 1]). Compositional zonation is absent in clinopyroxenes. Calculated Fe-Mg exchange coefficients (K_D) vary between 0.34 and 0.75, above the equilibrium value of 0.28 ± 0.08 (Putirka, 2008; Fig. S2). Equilibrium melts calculated following Higgins et al. (2022) yielded melt compositions of 57–68 wt% SiO_2 for amphibole and pyroxene gabbros from the gabbro and meladiorite units (Table 2).

4.4.2. Orthopyroxene

Mg# ranges from 0.4 to 0.66 in orthopyroxene. Amphibole gabbros have higher Mg# (0.61–0.66; $n = 2$) than pyroxene gabbros (0.41–0.50; $n = 2$; Fig. S2). Calculated Fe-Mg exchange coefficients (K_D) are higher than equilibrium K_D values, ranging between 0.56 and 1.22 (Fig. S2). Several transects through individual grains show no zonation in orthopyroxene.

4.4.3. Amphibole

Primary magmatic green amphiboles are magnesio- and ferri-hornblendes. Secondary brown, magmatic amphiboles replacing pyroxenes are dominantly tschermakites. Actinolite occurs in samples that show widespread alteration and are interpreted as deuteric (e.g., Werts et al., 2020). Amphibole Mg# ranges from 0.22 to 0.78 (Fig. S2). Amphiboles from the lower gabbro sample deformed in the BMFZ (sample BRGIC13) yield lower Mg# (0.58–0.66) compared to upper gabbro samples (0.61–0.78). Amphiboles from an upper gabbro adjacent to a felsic segregation have Mg# between that of the felsic segregation and upper gabbro amphiboles, corresponding to the transition from green primary magmatic amphiboles (segregation) to brown secondary magmatic amphiboles (gabbro) observed in thin section. Amphibole grains from the felsic hosts in the mingling zone have lower Mg# (0.22–0.63) compared to those of mafic enclaves (0.51–0.69; Fig. S2). Most amphiboles from the granite and granophyre samples are actinolitic. Secondary magmatic amphiboles, replacing clinopyroxenes, from the lower and upper gabbro units yielded equilibrium melt SiO_2 contents between 62 and 77 wt%, using the Higgins et al. (2022) chemometer (Table 2). Felsic segregations containing primary magmatic amphiboles yielded melt compositions between 70 and 78 wt% SiO_2. The meladiorite unit yielded amphibole melt compositions between 73 and 78 wt% SiO_2. Upper GIC units, including the mingling zone, granite, and granophyre, produced calculated amphibole melt compositions with SiO_2 contents between 72 and 78 wt% (Table 2).

4.4.4. Feldspar

Plagioclase is predominantly found in the gabbro, felsic segregations, and mingling zone. Alkali feldspar characterizes the upper felsic units and felsic segregations. Anorthite contents progressively decrease up-section through

TABLE 1. PETROGRAPHIC SUMMARY

Map unit	Major phase	Modal %*	Petrographic observations
Lower and upper gabbro	OL CPX OPX PL AMP BT	0–5 10–40 10–20 40–70 0–50 0–15	Fine (<1 mm) to medium grained (1–5 mm). Modal proportions vary: OL is restricted to lower gabbros; AMP and BT are more abundant in upper gabbros. PL is hypidiomorphic and aligned (Figs. 4A–4F). PX can show exsolution lamellae (Fig. 4E). Late-magmatic brown AMP replaces PX and occurs in interconnected space (red arrows in Fig. 4A); early-magmatic AMP is dark to light green (gabbro part in Fig. 4G). BT is late and commonly replaced by actinolite. Secondary epidote, chlorite, and actinolite replace PL and PX. Accessory minerals are Fe-Ti oxides, titanite, apatite, and zircon. Re-crystallization of AMP, secondary AFS, and ilmenite → titanite occurs in rocks from the BMFZ (Fig. 4F); minor solid-state deformation occurs outside the BMFZ (e.g., deformation twinning and undulose extinction in PL; white rectangles in Fig. 4B).
Felsic segregations	CPX AMP BT PL AFS QZ	0–5 5–20 5–20 0–30 20–80 20–30	Coarse grained (>0.5 cm); pegmatitic. Green AMP and brown BT are early magmatic. Accessory phases are apatite and zircon (≤0.3 mm; Fig. 4G). CPX is very rare. Graphic intergrowth of AFS and QZ is common (Fig. 4H). Myrmekite is rare. QZ and AFS display undulose extinction. At contact to surrounding gabbro, primary green AMP and BT are common; these gradationally transition into brown AMP replacing PX and absence of BT with increasing distance to contact.
Meladiorite	CPX AMP BT PL AFS QZ	0–30 0–40 0–20 0–40 0–50 0–20	Fine to coarse grained; heterogenous unit. Rock types range from PX- and AMP-gabbro (Fig. 4I) to AFS-granite (Fig. 4J). Brown AMP and BT are late-magmatic phases in gabbros (Fig. 4I). Diorite is most common, showing hypidiomorphic PL and poikilitic AMP with embayments (red arrows in Figs. 4K and 4L). Poikilitic AMPs in diorites are clustered (glomerocrysts; white rectangles in Fig. 4L) and themselves enclosed in poikilitic AFS and QZ (Figs. 4K and 4L). Accessory phases are Fe-Ti oxides, titanite, zircon, and apatite. Alteration minerals are chlorite, epidote, and actinolite (Fig. 4J); FSP is sericitized (Fig. 4J).
Mingling zone (mafic and felsic)	CPX AMP BT PL AFS QZ	0–5 10–30 10–20 0–10 10–30 5–20	Felsic part is medium to coarse grained; mafic part is fine grained (Fig. 4M). Titanite is a common accessory phase in felsic part. AMP is an early magmatic phase; BT replaces AMP but is also primary magmatic and interstitial. Other accessory phases are Fe-Ti oxides, zircon, and apatite. Rare PX occurs as core in AMP (mafic part). Secondary actinolite and epidote are present. FSP is sericitized; FSP is idiomorphic to hypidiomorphic (felsic part) and anhedral and interstitial (mafic part). Aligned PL and AMP occur in poikilitic QZ and AFS (Fig. 4N).
Granite and granophyre	CPX AMP BT PL AFS QZ	0–2 0–10 5–20 0–10 30–70 20–40	Fine to coarse grained (varies considerably). PX is rare as core in AMP. Accessory minerals are Fe-Ti oxides, titanite, zircon, and apatite. Alteration varies considerably: sericitized FSP, replacement of AMP and BT by chlorite, actinolite, and epidote. BT > AMP. Granites have equigranular texture (Fig. 4O). Granophyre unit is distinguished from underlying granite unit by the appearance of abundant granophyric intergrowth textures (>1 mm; Fig. 4P).

Notes: OL—olivine; CPX—clinopyroxene; OPX—orthopyroxene; PX—pyroxene; PL—plagioclase; AMP—amphibole; BT—biotite; AFS—alkali feldspar; FSP—feldspar; QZ—quartz; BMFZ—Bear Mountains fault zone.

*Modal percentages are estimated visually from thin sections; ranges reflect variability within each map unit. Uncertainties are ~10% of reported values.

the GIC, from An_{73} (anorthite end member component in plagioclase) in the upper gabbro unit, to An_{63} in the felsic segregations within the upper gabbro unit, to An_{32} in the meladiorite unit (Fig. S2). The mingling-zone plagioclase compositions are distinct, with the mafic enclaves containing cores and rims with An_{72}–An_{16} and the felsic host containing An_{36}–An_{12} (Fig. S2). Individual grains span a wide range in anorthite content, indicating compositional zoning within all units. Although rims generally have lower anorthite contents than cores, no simple core-rim zoning pattern occurs within most grains. All plagioclase data from the meladiorite and mafic mingling zone plot well above the lower-temperature An-Ab equilibrium boundaries, at K_D >0.3. Some felsic segregation plagioclases and felsic mingling zone plagioclases plot within the equilibrium zone. Equilibrium melt calculations (Scruggs and Putirka, 2018, equations 2 and 3) estimate SiO_2 melt compositions between 58 and >80 wt% (Table 2) and CaO contents <6 wt%.

4.5. Thermometry

Crystallization temperatures were calculated for pyroxene, amphibole, plagioclase, and titanite and compared to zircon crystallization temperatures reported in Ratschbacher et al. (2018). Results are shown in Figure 5 and reported in Table 2.

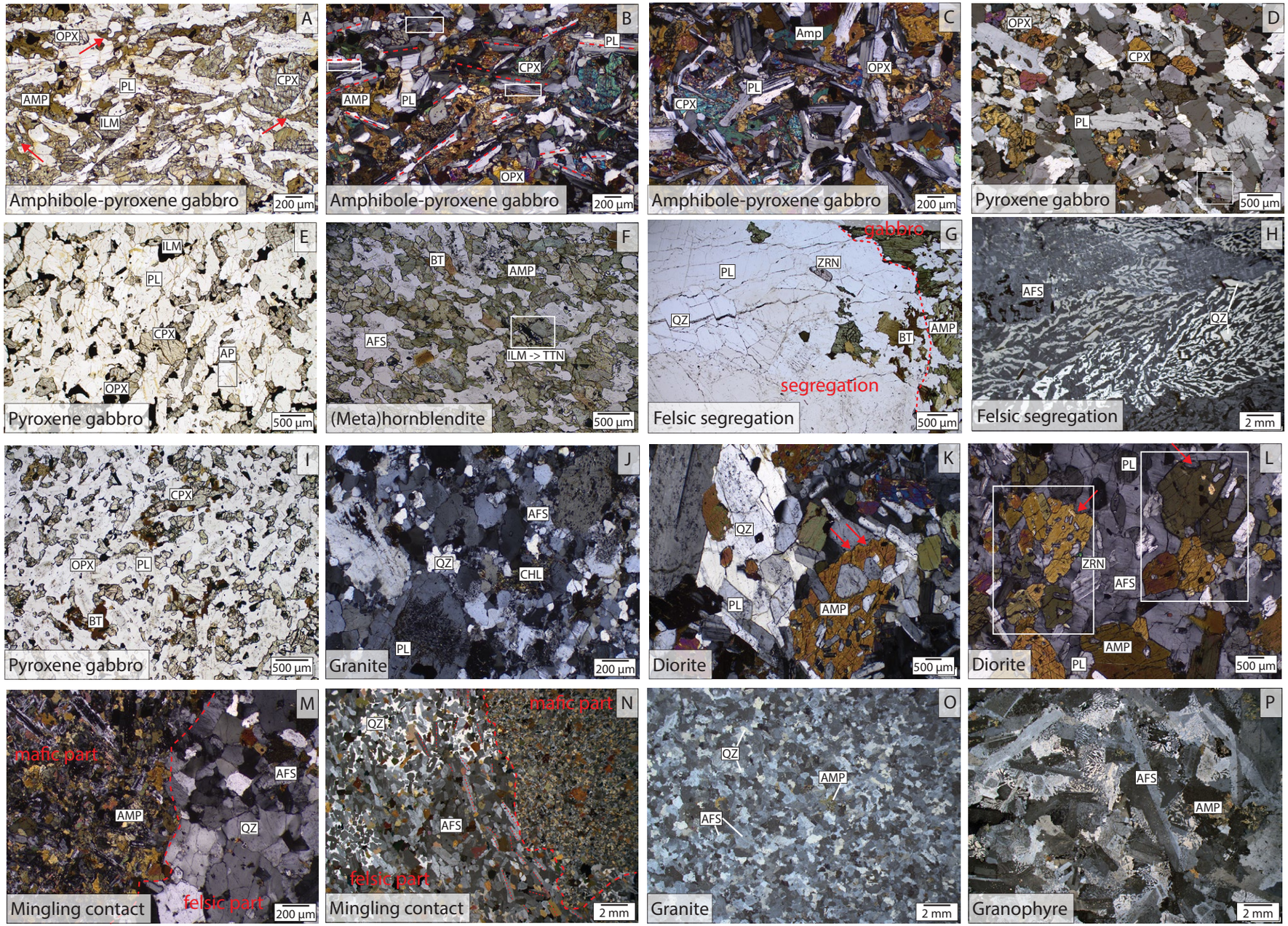

Figure 4. Thin-section images of rocks from different units of the Guadalupe Igneous Complex. (A–F) Gabbro unit. (A, B) Plane (A) and crossed (B) polarized views of the same area of an amphibole-pyroxene gabbro displaying alignment of plagioclase laths (red dashed lines), rare deformation twinning and undulose extinction (rectangles), and late-stage amphibole (red arrows). (C) Crossed polarized view of an amphibole-pyroxene gabbro without plagioclase alignment. (D, E) Crossed (D) and plane (E) polarized views of different areas of pyroxene gabbro; note the presence of deformation twinning in plagioclase (white rectangle) and exsolution lamellae in the central clinopyroxene grain in E. Also note small apatite crystals in black rectangle (E). (F) Plane polarized view of a deformed (meta-)hornblendite collected within the Bear Mountains fault zone. Black rectangle labeled ILM->TTN shows the replacement of ilmenite by titanite. (G, H) Felsic segregations in upper gabbro, plane (G) and crossed (H) polarized views of different areas; note the large grain sizes and intergrowth of feldspar and quartz. (I–L) Meladiorite unit: plane polarized view of a pyroxene gabbro (I) and crossed polarized views of a granite (J) and diorites (K and L). Note the embayments in amphiboles (red arrows in K and L) and clusters of amphiboles (white rectangles in L). (M, N) Mingling zone unit (different samples): crossed polarized view of a contact (thick red dashed line) between the felsic host and mafic enclaves. (N) Note alignment of plagioclase laths (thin red dashed lines) enclosed in quartz (white-yellow interference colors) and alkali feldspar (gray interference colors); (O, P) Granite and Granophyre unit: crossed polarized view of a granite (O) and granophyre (P). Note the granophyric texture in O. AFS—alkali feldspar; AMP—amphibole; AP—apatite; BT—biotite; CHL—chlorite; CPX—clinopyroxene; ILM—ilmenite; OPX—orthopyroxene; PL—plagioclase; QZ—quartz; TTN—titanite; ZRN—zircon.

TABLE 2. THERMOMETRY AND CHEMOMETRY

	Phase	Method reference	Map unit					
			Gabbro	Felsic segregation	Meladiorite	Mingling zone (mafic)	Mingling zone (felsic)	Granite and granophyre
Temperature range (°C)	CPX	Putirka et al. (1996)	1048–979	NA	NA	NA	NA	NA
		Putirka et al. (2003)	1011–989	NA	NA	NA	NA	NA
		Higgins et al. (2022)	1037–942	933	1033–900	NA	NA	NA
	OPX	Köhler and Brey (1990)	1198–809	NA	1195–890	NA	NA	NA
	PL	Putirka (2005)	1226	1210–870	NA	NA	1072–979	869
		rhyoliteMELTS	1020–990	940–910	990–950		870–820	
	AMP	Putirka (2016)	949–687	860–719	891–698	775–694	791–642	672–619
		Higgins et al. (2022)	850–776	962–756	850–776	830–738	850–738	776–738
	ZRN	Ferry and Watson (2007)	871–641	797–621	842–694	NA	NA	888–649
	TTN	Hayden et al. (2008)	722–635	NA	NA	NA	751–639	783–646
Melt SiO_2 (wt%)	CPX	Higgins et al. (2022)	57–68.1	NA	58.8–68.7	NA	NA	NA
	AMP	Higgins et al. (2022)	61.9–77.1	70.7–77.5	73.5–77.1	75.4–78.2	72.6–78.3	76.9–78
	PL	Scruggs and Putirka (2018)	59.4–78.7	63.4–83.1	74.8–77.7	59.9–80.9	73.2–82.4	59.2

Notes: NA—not available; CPX—clinopyroxene; OPX—orthopyroxene; PL—plagioclase; AMP—amphibole; ZRN—zircon; TTN—titanite; rhyoliteMELTS—Gualda et al. (2012).

4.5.1. Clinopyroxene and Orthopyroxene

Clinopyroxene crystallization temperatures agree across methods in the upper gabbro unit, clustering at 1000 °C. The meladiorite unit shows clinopyroxene crystallization temperatures clustering at 960 °C. The Ca-in-orthopyroxene thermometer yielded crystallization temperatures >900 °C in both the upper gabbro and meladiorite units, corresponding to petrographic observations that orthopyroxene is an early crystallization phase.

4.5.2. Amphibole

The amphibole-only thermometer of Putirka (2016) yielded crystallization temperatures ranging from 950 to 750 °C in lower mafic units and 780–620 °C temperatures in intermediate and felsic upper units. These temperatures show general agreement with estimates using the machine learning calibration method of Higgins et al. (2022) for lower mafic and intermediate GIC units, but the Higgins et al. (2022) thermometer predicts significantly higher temperatures (>750 °C) than Putirka (2016) for the upper GIC units.

4.5.3. Plagioclase

Calculations using Putirka (2005, equation 2) produced plagioclase crystallization temperatures that decrease upwards in the GIC but at unusually high temperatures relative to other minerals in the assemblage (1100–1200 °C). These estimates were compared to rhyolite-MELTS models. In the upper gabbro, models produced $An_{73–67}$ plagioclase at 1020–990 °C, which corresponds to the highest anorthite content found in the upper gabbro samples, and the model recreated the approximate (high-temperature, near liquidus) crystallization sequence observed in thin sections. Modeled plagioclase crystallization temperatures in the felsic segregations are slightly lower at 940–910 °C with good agreement between clinopyroxene- and amphibole-liquid models. The meladiorite results are comparable to those from the upper gabbro, with plagioclase crystallization temperatures modeled at 950–990 °C, producing $An_{68–66}$ plagioclase. This is more calcic than found in the meladiorite samples, but thin section observations suggest plagioclase cores have experienced alteration. The mingling zone, granite, and granophyre units produced similar plagioclase crystallization temperatures in rhyolite-MELTS, between 870 and 820 °C. The models in this case produced quartz at high temperatures and could not reproduce high-temperature phases. This may be due to the reliance on amphibole-equilibrium melts (no clinopyroxene found) and the poor reproducibility of amphibole in MELTS models. Anorthite contents predicted by the model also showed some mismatch compared to natural samples. For example, the mingling zone model produced An_{50} plagioclase, but the most calcic plagioclase measured is An_{36}. The model could not reproduce the calcic plagioclase grains (An_{71}) in the mafic mingling zone end member, and we suspect this is due to inheritance. Rhyolite-MELTS models were also used to estimate liquidus temperatures for each unit, showing a general decrease in temperature between the lower and the upper units.

4.5.4. Titanite

Titanite crystallization temperatures yielded temperatures from 780 °C to the solidus in the upper gabbro, mingling zone, and granite units.

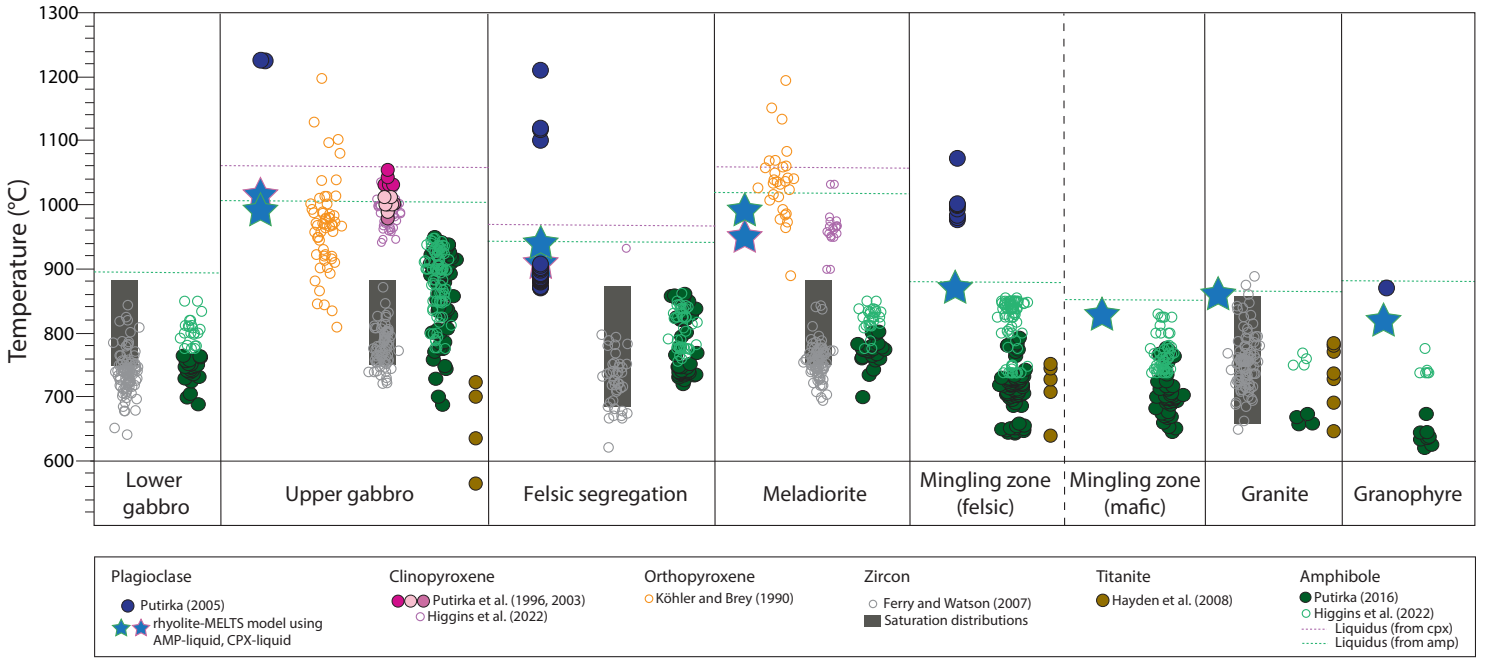

Figure 5. Crystallization temperatures recorded in Guadalupe Igneous Complex units, estimated from mineral thermometry and rhyolite-MELTS modeling. Colors represent different minerals, and symbols represent different methods (listed in figure). *Plagioclase:* Crystallization temperatures are calculated using Putirka (2005, equation 23) for plagioclase anorthite content >10 in equilibrium with whole-rock compositions in the upper gabbro (1 sample), felsic segregations (2 samples), mingling zone felsic end member (2 samples), and granophyre (1 sample). Stars represent temperature of plagioclase crystallization calculated using rhyolite-MELTS models with starting compositions in equilibrium with a clinopyroxene (Cpx)–calculated liquid (purple rims) or amphibole (Amp)–calculated liquid (green rims). See text for details. *Clinopyroxene:* Crystallization temperatures are calculated using Putirka et al. (1996, equations T1 and T2), Putirka et al. (2003), and Higgins et al. (2022) for the upper gabbro (4 samples), felsic segregation (1 sample), and meladiorite (1 sample). *Orthopyroxene:* Crystallization temperatures are calculated using Köhler and Brey (1990) in the upper gabbro (5 samples) and the meladiorite unit (5 samples). *Zircon:* Crystallization temperatures are calculated using Ferry and Watson (2007) Ti-in-zircon method (equation 15) and zircon saturation distributions from Ratschbacher et al. (2018). *Titanite:* Crystallization temperatures are calculated using Hayden et al. (2008, equation 7) for one sample each in the upper gabbro, mingling zone felsic end member, and granite units. *Amphibole:* Crystallization temperatures are calculated using Putirka (2016, equation 5) and Higgins et al. (2022) for the lower gabbro (1 sample), upper gabbro (5 samples), felsic segregations (4 samples), meladiorite (6 samples), mingling zone mafic and felsic end members (4 samples each), granite (3 samples), and granophyre (1 sample). Liquidus temperatures calculated from rhyolite-MELTS are shown in dashed lines for Cpx-calculated liquids (purple) and Amp-calculated liquids (green), using the calculated liquid with the lowest SiO_2 composition as the starting composition (see text for details). Uncertainties of calculations are listed in Table S6 (see text footnote 1).

4.5.5. Zircon

The Ti-in-zircon thermometer of Ferry and Watson (2007) was used to calculate zircon crystallization temperatures in addition to the calculation of zircon saturation distributions (see Ratschbacher et al., 2018, for details). Temperatures cluster across an interquartile range of 30–70 °C but span a much larger range from 890 to 650 °C. Figure 5 illustrates the relative shift in crystallization temperature between the major and accessory minerals studied. Initially, zircon crystallized at lower temperatures (i.e., later) relative to early plagioclase, pyroxene, and amphibole (where available) within the gabbro units and the felsic segregations. In contrast, zircon is an early phase relative to amphibole and plagioclase in the meladiorite and granite units.

4.6. Whole-Rock Sr-Nd Isotopes

Whole-rock initial $\varepsilon_{Nd(149\ Ma)}$ (ε_{Ndi}; where the subscript $_{(149\ Ma)}$ indicates age-corrected values) and initial $^{87}Sr/^{86}Sr_{(149\ Ma)}$ (Sr_i; where the subscript $_{(149\ Ma)}$ indicates age-corrected values) values of 13 samples from the GIC vary between +7.02 and +2.13 and between 0.7026 and 0.7069, respectively (Fig. 6). There is

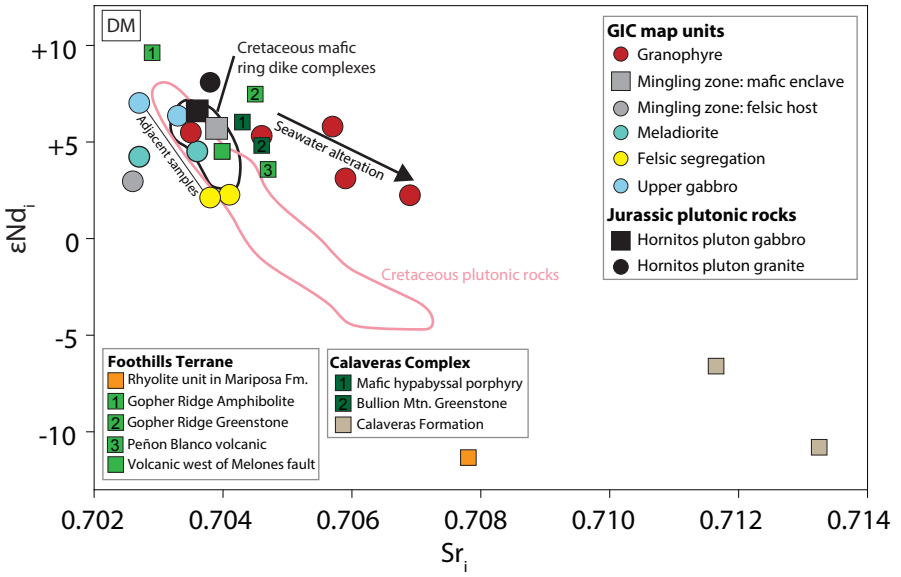

Figure 6. Age-corrected radiogenic isotopes of the Guadalupe Igneous Complex (GIC), the Hornitos pluton, one rhyolite sample exposed in the Mariposa Formation, and metasedimentary and metavolcanic rocks from the Foothills terrane and the Calaveras Complex. Foothills terrane samples analyzed in this study are labeled 1–3; Calaveras Complex samples analyzed in this study are labeled 1–2. For locations, see Figure 1. Other Western Metamorphic Belt samples (one volcanic sample west of the Melones fault zone, exact location unknown; and two Calaveras Formation samples, locations unknown) are from DePaolo (1981). Cretaceous plutons in the vicinity of the GIC include the Fine Gold Intrusive Suite and the Academy pluton (Lackey et al., 2012; Truschel, 1996; Masi et al., 1981; Bateman et al., 1992). Mafic ring dike complex data are from Clemens-Knott (1992). DM—depleted mantle after Zindler and Hart (1986).

no systematic variation in ε_{Ndi} and Sri_i values from the base to the top of the GIC. The upper gabbro and felsic segregation samples (BRGIC10 and 10D), collected in close proximity, differ in ε_{Ndi} values by 4.90 and in Sri_i values by 0.001 ("Adjacent samples" in Fig. 6). All samples except two samples from the granophyre unit show values of Sri_i <0.706, consistent with the GIC's location west of the $^{87}Sr/^{86}Sr$ 0.706 line (Kistler and Peterman, 1973; Kistler, 1990). Three samples from the granophyre unit show a trend toward increasing Sri_i with slightly decreasing ε_{Ndi} values similar to trends observed in mid-ocean-ridge basalt (MORB) affected by seawater alteration (Hart et al., 1974; Fig. 6). One 152 Ma rhyolite sample collected directly east of the granophyre unit (Fig. 2) has a $\varepsilon_{Nd(152\ Ma)}$ value of –11.33 and a $Sri_{(152\ Ma)}$ value of 0.7078 (Fig. 6). Five samples collected from several units of the Foothills terrane and Calaveras Complex analyzed in this study (Fig. 1) yielded $\varepsilon_{Nd(152\ Ma)}$ values from +9.63 to +3.55 and $Sri_{(152\ Ma)}$ values from 0.7029 to 0.7047 (Fig. 6). For comparison, Figure 6 shows data from the Jurassic Hornitos pluton (this study) and published data from Cretaceous plutonic rocks (pink outline), Cretaceous mafic ring dike complexes (black outline), two samples from the Calaveras Formation (brown squares), and one sample from a volcanic rock west of the Melones fault (light green square; see figure captions for references).

4.7. Whole-Rock Oxygen Isotopes and Major Element Compositions

Whole-rock $\delta^{18}O$ [$\delta^{18}O_{(whole\text{-}rock)}$] values in the GIC vary from +5.47‰ to +8.57‰ (Figs. 7 and 8) and show an increase from the lower gabbro to the meladiorite unit (Fig. 8). Granophyre $\delta^{18}O_{(WR)}$ values depart from the generally upward increase in $\delta^{18}O$ with increasing stratigraphic position, having values that are lower (+5.74‰ and +7.01‰) than those of the units immediately below (Fig. 8).

A detailed transect of 21 samples, collected perpendicular to compositional layering in the lower to upper gabbros (Shultz Mountain area; Fig. 7A; "sample transect" in Fig. 2), shows a variation in $\delta^{18}O_{(WR)}$ values from +5.47‰ to +7.24‰ (Fig. 7B). Although scatter is observed, the lowest $\delta^{18}O_{(WR)}$ values are from the base of the transect and increase by ~2‰ up stratigraphy (Fig. 7B). This correlates with a decrease in whole-rock Mg# values from ~75 to 65 in the lower gabbros and an abrupt shift to lower values in the upper gabbros (Fig. 7C).

Mariposa Formation host rock $\delta^{18}O_{(WR)}$ values at the base of the GIC in the BMFZ are low (+4.31‰ to +5.95‰) compared to the host rock sample collected ~1 km north of the GIC (+12.12‰; Figs. 2 and 8). The $\delta^{18}O_{(WR)}$ values of this Mariposa Formation sample is similar to $\delta^{18}O_{(WR)}$ averages of ~13‰ in the Mariposa Formation from farther north (Boehlke and Kistler, 1986).

4.8. Oxygen Isotopes in Zircon

Zircons from the lower and upper gabbro units show overlapping oxygen isotope compositions (+3.8‰–+4.6‰), below the value for mantle-derived zircons (+5.3‰ ± +0.3‰; Valley et al., 1998; Fig. 9). Zircons from the granite and meladiorite samples show values above the mantle value, between 5.6‰ and 6.6‰, while values from the felsic segregation zircons (+4.8‰–+5.4‰) mostly overlap with the mantle values (Fig. 9). Zircon $\delta^{18}O$ trends upward with

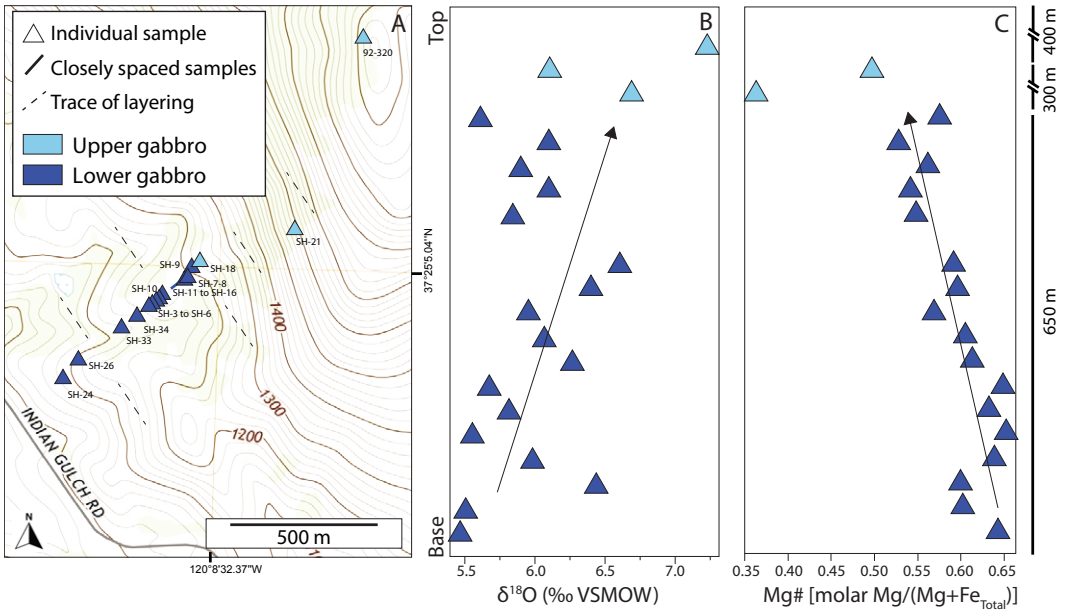

Figure 7. Whole-rock $\delta^{18}O$ ($\delta^{18}O_{(WR)}$) values in samples from the gabbro unit collected along a transect perpendicular to compositional layering (for location of transect, see Fig. 2). (A) Map of sample locations. Topographic contour interval 20 feet. (B, C) $\delta^{18}O_{(WR)}$ values (B) and Mg# [molar MgO/(MgO + FeO_{total})] (C) plotted relative to their approximate position in the transect. Black arrows indicate trends up-section. VSMOW—Vienna standard mean ocean water.

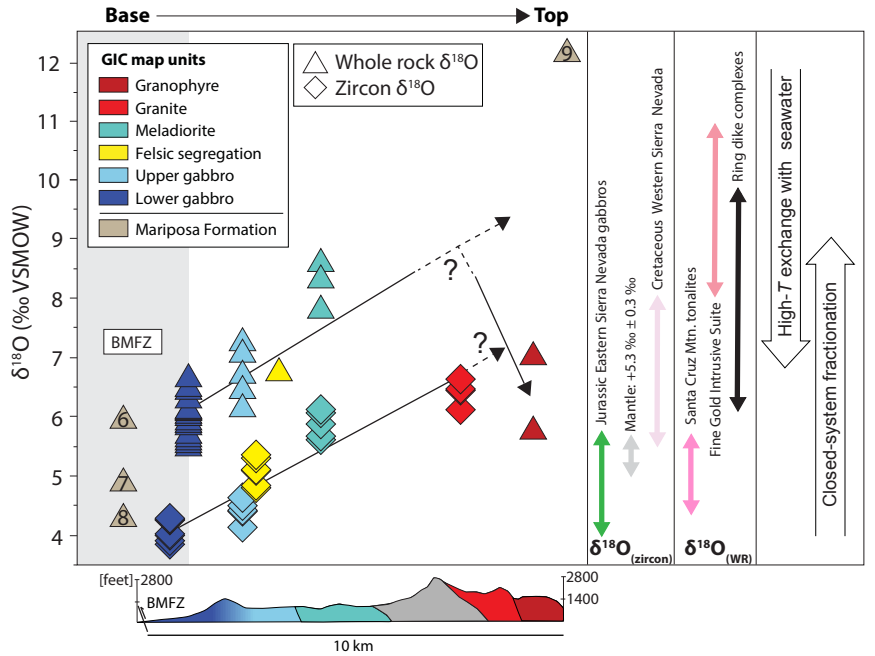

Figure 8. Whole-rock ($\delta^{18}O_{(WR)}$) and zircon ($\delta^{18}O_{(zircon)}$) oxygen isotope compositions of Guadalupe Igneous Complex (GIC) and Mariposa Formation samples (numbers in triangles correspond to locations on map in Fig. 1). $\delta^{18}O_{(WR)}$ and $\delta^{18}O_{(zircon)}$ values are plotted versus approximate position relative to the base and top of the GIC. Black indicates potential trends with stratigraphic position from the base to the top of the complex. Right panels: $\delta^{18}O_{(zircon)}$—range of Jurassic Eastern Sierra Nevada gabbro values is from Gevedon (2013) and Gevedon and Clemens-Knott (2013), range of mantle values is from Valley et al. (1998), and range of Cretaceous Western Sierra Nevada values is from Lackey et al. (2008); $\delta^{18}O_{(WR)}$—range of mylonite tonalites from the Santa Cruz Mountain pluton is from Tobisch et al. (1991), range of Cretaceous plutonic rocks from the Fine Gold Intrusive Suite (Bass Lake Tonalite) is from Lackey et al. (2012), and range of mafic ring dike complexes is from Clemens-Knott (1992). Arrows on far right indicate potential trends of oxygen isotope values if following closed-system fractionation (increase in $\delta^{18}O$ values) or affected by high-temperature (high-*T*) exchange with seawater (decrease of $\delta^{18}O$ values). VSMOW—Vienna standard mean ocean water. BMFZ—Bear Mountains fault zone.

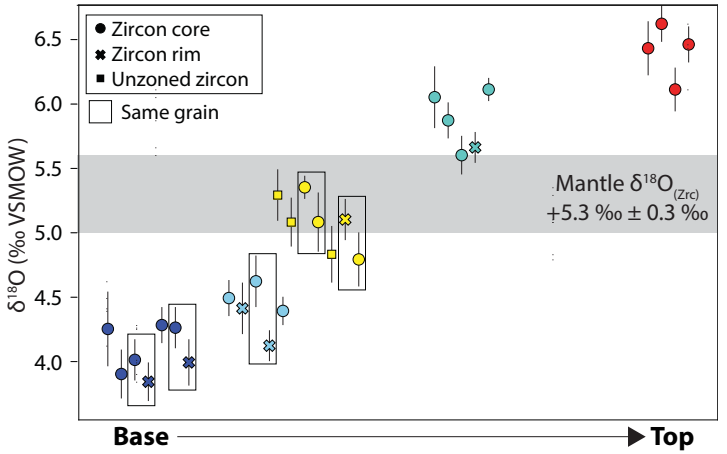

Figure 9. Single spot analyses of oxygen isotope compositions of zircon cores, rims, and unzoned grains from the Guadalupe Igneous Complex (GIC) plotted versus approximate position relative to the base and top of the GIC. Mantle $\delta^{18}O_{(zircon)}$ values are from Valley et al. (1998). Error bars show 2σ uncertainties. Color coding is the same as in Figure 8. VSMOW—Vienna standard mean ocean water.

stratigraphic position: At the base of the GIC (gabbros), the zircons show sub-mantle isotope compositions, whereas at the top (granite), the zircons record elevated oxygen isotope compositions. This upward increase in zircon $\delta^{18}O$ values mirrors the upward increase in whole-rock $\delta^{18}O$ values (Fig. 8). Zircon grains show an intra-sample range in $\delta^{18}O$ of as much as 0.5‰ (Fig. 9).

A comparison to zircon $\delta^{18}O$ values from Late Jurassic gabbros of the Eastern Sierra Nevada (Gevedon, 2013; Gevedon and Clemens-Knott, 2013; green arrow in Fig. 8) show similarly low zircon $\delta^{18}O$ values to GIC gabbros. A compilation of $\delta^{18}O_{(zircon)}$ values of Cretaceous plutons in the Western Sierra Nevada (Lackey et al., 2008; light pink arrow in Fig. 8) reveals that the GIC gabbros have lower zircon $\delta^{18}O$ values. In addition, GIC $\delta^{18}O_{(zircon)}$ values are lower than typical mantle values obtained in Cretaceous gabbros in the Western Sierra Nevada (Fu et al., 2008; Lackey et al., 2008, 2012).

4.9. Zircon Trace Element Geochemistry

Zircon trace element variations occur at the grain, hand sample, and pluton scales. At the grain scale, zircon rims from the lower gabbro and meladiorite units have higher Yb/Dy but lower Th/U ratios and show higher Hf concentrations compared to grain interiors (Figs. 10A–10B and 10G–10H). Rim compositions of unpolished zircons from the lower and upper gabbro correspond to rims on polished grains (Fig. 10). Zircons from the gabbro of the meladiorite unit show a positive correlation between Hf and Yb/Dy and a negative correlation between Hf and Th/U and between Hf and Ti (Figs. 10G–10I). Zircons from the upper and lower gabbro show a weak positive correlation between Hf and Yb/Dy (Figs. 10A and 10D). Zircons from the felsic segregation (Figs. 10J–10L) do not show systematic core-rim compositional relationships, while zircons for the granite sample show slightly higher Yb/Dy in the rims compared to cores (Fig. 10M). The intra-grain compositional range observed in the mafic unit and felsic segregation samples is larger than in the zircons from the granite. Figure S3 (see footnote 1) shows the difference in the minimum and maximum values of Hf concentrations and Yb/Dy within single zircons analyzed from each sample. These variations in intra-grain composition do not correlate with a zircon CL-specific zonation type.

Although compositional overlap exists at the hand-sample scale, the zircons from the upper gabbro unit can be distinguished from the zircons in the lower gabbro unit by slightly higher Ti contents and Lu/Hf and lower Hf concentrations and Yb/Dy (Figs. 11A–11C). Zircons from the felsic segregation sample have higher Hf concentrations and Yb/Dy and lower Ti contents than the zircons of the adjacent upper gabbro sample (Figs. 11A–11C). Zircons from the gabbro of the meladiorite unit are dissimilar to the other gabbro zircons in having generally higher Yb/Dy and lower Th/U (Figs. 10 and 11). Zircons from the granite sample have the lowest Eu/Eu* ($[Eu_N/(Sm_N \times Gd_N)^{0.5}]$; N indicates normalization to chondritic values; Fig. 11D); their Hf content is similar to that of the rhyolite zircons (Fig. 11). The latter have higher Eu/Eu* (Fig. 11D), but the Ti contents and element ratios overlap with those of the granite unit zircons (Figs. 11A–11C). The zircons of the felsic segregation sample have distinctively higher Yb/Dy than the majority of zircons from the other samples (Fig. 11C). Figure 11 also shows that the mafic zircons and the zircons from the felsic segregation sample span a wider compositional range than the zircons from the granite and rhyolite samples.

On the pluton scale, the Eu anomalies (Eu/Eu*) are increasingly more pronounced from the lower gabbro to the granite unit (Fig. 11D); this corresponds with decreasing ages and correlates with the whole-rock composition trend: More mafic and older samples have higher Eu/Eu* compared to younger and more felsic samples.

To better understand the observed geochemical range in zircon trace elements, we conducted coupled major and trace element modeling integrated with accessory phase saturation calculations using Perple_X (Connolly 2005, 2009) and StatGeochem.jl (Keller, 2021). This allows estimation of the composition of zircon expected to crystallize from the interstitial melts resulting from equilibrium bulk crystallization of each whole-rock composition. As demonstrated in previous sections, the majority of early-crystallizing mineral phases are not in equilibrium with their whole-rock composition, thus whole-rock compositions cannot be equated to melt compositions. However, by using respective whole-rock compositions, we can predict what the zircon compositions would be given closed-system equilibrium crystallization and compare that with observed compositions. We first conducted equilibrium batch crystallization calculations from liquidus to solidus using the thermodynamic modeling program Perple_X (Connolly 2005, 2009) and the following melt and solid solution models: melt (Holland et al., 2018); clinoamphibole and clinopyroxene (Green et al., 2016); olivine, orthopyroxene, spinel, and garnet

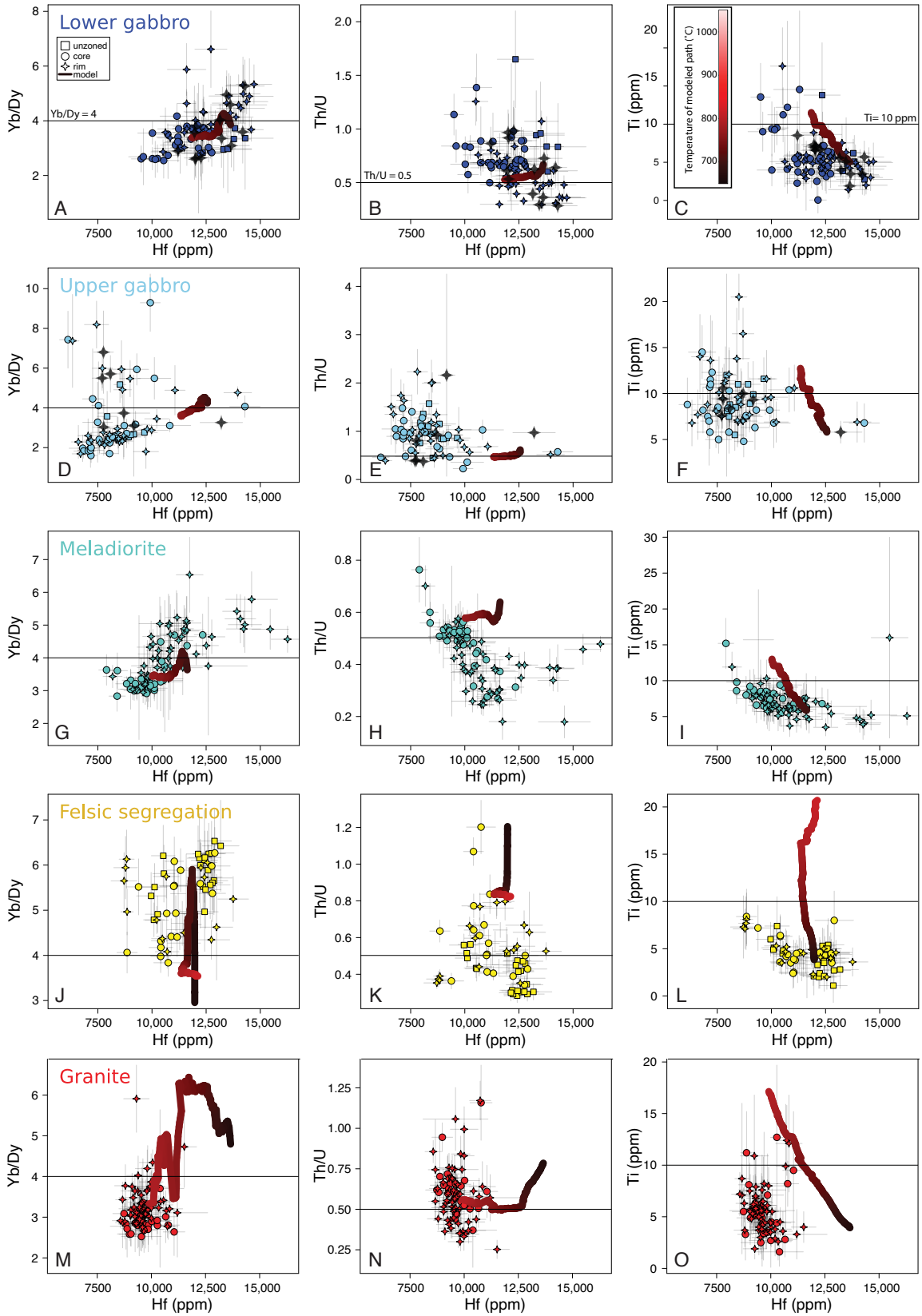

Figure 10. Zircon trace element composition in cores and rims of zircons from mafic and felsic samples from the Guadalupe Igneous Complex. (A–C) (Meta-)hornblendite from lower gabbro unit. (D–F) Amphibole-pyroxene gabbro from upper gabbro unit. (G–I) Pyroxene gabbro from meladiorite unit. (J–L) Felsic segregation. (M–O) Granite from granite unit. Color-coded line represents modeling results (see text for explanation). Gray symbols are analyses from unpolished zircon grains in the lower and upper gabbro sample. Horizontal lines in each vertical set of panels marks an equal ratio (e.g., for panels A, D, G, J, and M, the horizontal lines marks a Yb/Dy ratio of 4); note that the x axis in each panel has the same scale. Error bars show 2σ uncertainties.

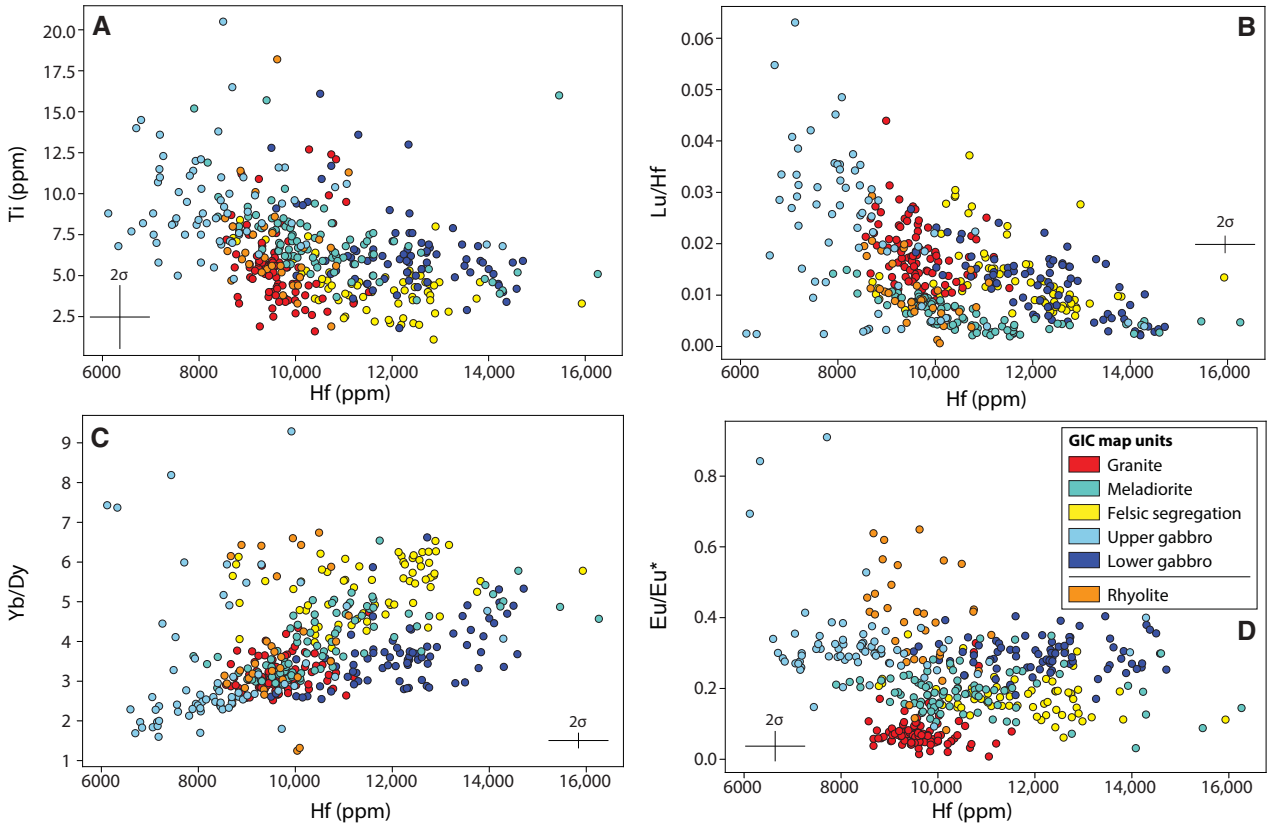

Figure 11. Trace element compositions of zircons from the Guadalupe Igneous Complex (GIC). (A) Hf versus Ti; (B) Hf versus Lu/Hf; (C) Hf versus Yb/Dy; (D) Hf) versus Eu/Eu* [$Eu_N/(Sm_N \times Gd_N)^{0.5}$]. N indicates normalization to chondritic values. Error bars show 2σ uncertainties.

(Jennings and Holland, 2015); and mica (White et al., 2014), with the internally consistent end-member thermodynamic database of Holland and Powell (2011) at a pressure of 3 kbar and 4 wt% H_2O. Using the resulting modal abundances of each solid phase and melt, we then conducted trace element partitioning calculations using the composition-dependent partition coefficient data set of Keller (2021), compiled via the Geochemical Earth Reference Model (GERM) Partition Coefficients Database (https://kdd.earthref.org/KdD/). With these melt trace element compositions and temperatures, we then applied the zircon saturation model of Boehnke et al. (2013), the apatite saturation model of Harrison and Watson (1984), the sphene model of Ayers et al. (2018), and the monazite saturation model of Montel (1993). Because the saturation of several of these accessory phases depends on trace elements that also partition into other accessory phases, bulk solid-melt partition coefficients and melt trace element compositions were updated iteratively after adding each accessory phase. Trace element concentrations in model zircon were calculated using the final melt trace element compositions and temperatures and the temperature-dependent partition coefficients of Claiborne et al. (2018). Finally, Ti in model zircon was calculated using the Ti-in-zircon relation of Ferry and Watson (2007) with melt Ti activities checked against the rutile saturation model of Hayden and Watson (2007). Results are shown as modeled paths in Figure 10.

5. DISCUSSION

In this study, we present a combination of (1) textural observations, (2) mineral-whole rock equilibrium calculations, (3) mineral chemometric

calculations, (4) zircon trace element geochemistry and modeling, and (5) pluton-scale Sr-Nd, $\delta^{18}O_{(WR)}$, and $\delta^{18}O_{(zircon)}$ isotope data that together indicate that open-system magmatic and sub-solidus processes operated at all scales to create the observed chemical and isotopic characteristics of the GIC. In the following discussion, we provide evidence for this interpretation by first discussing the isotopic and chemical signatures that were acquired below the emplacement level and then the signatures acquired at the emplacement level from the outcrop scale to the pluton scale. Finally, we integrate the outcomes of this study with published geochronology to present a new conceptual model of the evolution of the GIC.

5.1. Isotopic and Chemical Characteristics Acquired below the Emplacement Level

Mineral chemometric calculations of early-crystallizing phases (e.g., pyroxene) indicate that melts arriving in the GIC were at least andesitic in composition (≥58 wt% SiO_2; Table 2) and did not represent direct mantle-derived primary magmas. An additional differentiation step would have been required below the emplacement level to generate intermediate melts of ≥58 wt% SiO_2.

GIC Sr-Nd isotope compositions are regionally consistent with their spatial position in the western foothills of the Sierra Nevada arc. Plutons and volcanic rocks in this region, west of the Foothills suture and the $^{87}Sr/^{86}Sr_i$ 0.706 line, display a juvenile, largely mantle-derived isotopic signature, modified by intrusion into a pre-existing arc basement of oceanic and distal continental affinity sediments (Kistler and Peterman, 1973) that include hydrothermally altered materials (Lackey et al., 2008). A comparison to other mafic complexes in the foothills, such as the Cretaceous mafic ring dike complexes (Clemens-Knott, 1992) further south, shows that the GIC Sr-Nd isotope compositions are similar (Fig. 6). However, the GIC shows slightly lower $\delta^{18}O_{(WR)}$ values at low-SiO_2 (gabbro) compositions compared to the Cretaceous mafic ring dike complexes and lower $\delta^{18}O_{(WR)}$ values compared to other Cretaceous plutonic rocks ($\delta^{18}O_{(WR)}$ panel in Fig. 8). Additionally, GIC gabbro $\delta^{18}O_{(zircon)}$ values are lower than typical mantle values and $\delta^{18}O_{(zircon)}$ values obtained from Cretaceous gabbros in the Western Sierra Nevada (Fu et al., 2008; Lackey et al., 2008, 2012; $\delta^{18}O_{(zircon)}$ panel in Fig. 8). The low $\delta^{18}O$ values observed in whole rocks and zircons from GIC gabbros can be explained by either (1) an enriched source with unusually low $\delta^{18}O$ values present in the Jurassic but not in the Cretaceous Sierra Nevada arc, and/or (2) assimilation of high-temperature, hydrothermally altered material (either bulk assimilation or assimilation of partial melts of altered material). Late Jurassic to Early Cretaceous gabbros from the Eastern Sierra Nevada show similarly low $^{18}O_{(zircon)}$ values (Gevedon, 2013; Gevedon and Clemens-Knott, 2013; Fig. 8). Thus, mafic magmas in the Late Jurassic arc might have re-worked earlier Jurassic marine sediments that had been hydrothermally altered along arc-wide shear zones, such as the BMFZ. Studies specifically targeting Late Jurassic mafic rocks are required to further test the possible presence of a low-$\delta^{18}O$ source and the extent of alteration in the Late Jurassic arc. Assimilation of pre-existing hydrothermally alerted crust is commonly invoked to explain low-$\delta^{18}O$ magmas (e.g., Bindeman et al., 2008; Troch et al., 2020). Bulk assimilation of host rock units is not observed at the emplacement level (e.g., there is an absence of stoped blocks and host rock xenoliths), thus if present, such assimilation must have occurred below the emplacement level and/or during ascent. Contamination of rocks from the Calaveras Complex, east of the Melones fault zone, is excluded due to their distinctively more radiogenic isotope composition (i.e., Calaveras Formation; Fig. 6) and their fault-separated location in another terrane (Fig. 1). The Mariposa Formation wall rocks have a similar Sr_i isotopic composition (0.7047 and 0.7046, respectively; Lackey et al., 2012) to the GIC magmatic Sr_i values (0.7026–0.7046) but higher $\delta^{18}O_{(WR)}$ values (Fig. 8). However, at the base of the GIC in the BMFZ, Mariposa Formation $\delta^{18}O_{(WR)}$ values are as low as +4.3‰ (Fig. 8), indicating the influence of high-temperature exchange with meteoric water and/or seawater. Given the proximity of the BMFZ to the gabbro unit (Fig. 1) and the presence of migmatites in the BMFZ at the base of the GIC (Fig. 3A), bulk assimilation or assimilation of partial melts of hydrothermally altered Mariposa Formation might account for the low $\delta^{18}O_{(WR)}$ and $\delta^{18}O_{(zircon)}$ of GIC gabbros.

5.2. Isotopic and Chemical Characteristics Acquired at the Emplacement Level

5.2.1. Zircon Crystallization in Mafic and Felsic Rocks

Equilibrium partitioning of trace elements between zircon and melt is a function of temperature and melt composition (e.g., Claiborne et al., 2018). Because the start of zircon crystallization in mafic and felsic samples occurred at similar temperatures, ~880 and ~865 °C, respectively (Fig. 5; Ratschbacher et al., 2018), we interpret the differences in trace element composition of zircon from the mafic and felsic samples as a function of changing melt composition and not temperature. Zircon Hf concentration can be used as an indicator of magmatic differentiation and melt evolution (Hoskin and Schaltegger, 2003; Claiborne et al., 2006). Zircons from the lower gabbro and meladiorite units show a wide range in Hf concentrations that are generally greater than those of the granite and rhyolite samples (Fig. 11). This is counterintuitive, given that zircon from felsic rocks should record more evolved and thus higher Hf concentrations (e.g., Hoskin and Schaltegger, 2003). This can be reconciled if zircon in the mafic samples crystallized later relative to the major phases (e.g., pyroxene, feldspar, amphibole; Fig. 5). None of these major phases incorporate significant amounts of Hf, thus the high Hf concentrations in the mafic samples can be explained by late-stage zircon saturation and growth in interstitial melts that were highly enriched in Hf. Ratschbacher et al. (2018) determined that >80% bulk crystallization occurred prior to zircon saturation in the mafic samples (as opposed to ~10% bulk crystallization in felsic samples). Thus, at 80% crystallinity, zircon in the mafic samples likely crystallized from residual, interstitial melt pools recording the latest stages of crystallization.

Zircon from mafic samples that crystallized from late-stage melts should display a small compositional range, but the opposite is observed (Figs. 10 and 11): For example, zircons from the granite sample show a much narrower compositional range in Hf concentrations and Eu/Eu* than the zircons from mafic samples (e.g., Fig. 11D). Perple_X modeling in combination with zircon trace element partitioning calculations shows that closed-system crystallization in mafic samples, taking the whole-rock composition as a parental liquid approximation (although this is not a good approximation—see section 5.2.3. below), produces a much narrower range in zircon trace element compositions than is observed in the data (Fig. 10). Consequently, we infer that the observed large range in zircon trace element compositions is not the result of a single differentiation path but rather the consequence of zircon crystallization from diverse interstitial melts, collected from an area within the gabbro crystal mush larger than the felsic segregation–upper gabbro sample distance (~1 m). This implies that the gabbro crystal mush was constructed from multiple magma batches with slightly different melt compositions and degrees of differentiation and that the interstitial melt was probably able to percolate through the mush, seen at the mesoscale through felsic segregations.

5.2.2. Crystal-Mush Processes: Formation of Felsic Segregations

Previous work using whole-rock chemistry (Putirka et al., 2014) and high-precision U-Pb zircon geochronology (Ratschbacher et al., 2018) indicates that the felsic segregations in the upper gabbro unit formed through fractional crystallization processes from the surrounding gabbro crystal mush. However, the felsic segregations and surrounding upper gabbro have distinct whole-rock Sr-Nd isotopic compositions and $\delta^{18}O_{(zircon)}$ values (Figs. 6 and 9), precluding closed-system fractionation of a single melt from the gabbro crystal mush. Models to explain the whole-rock Sr_i and ε_{Ndi} composition of the gabbro and adjacent felsic segregation include: (1) fractionation of an isotopically hybrid melt from an isotopically heterogeneous crystal mush (un-mixing trend; Beard, 2008); (2) selective accumulation of mineral phases that record different magmatic histories and isotopic ratios (e.g., Tepley and Davidson, 2003, their scenario 2), including isotopic zonation within phases (e.g., Tepley and Davidson, 2003, their scenario 3); (3) sub-solidus metasomatism or re-equilibration of isotopic composition in either the felsic segregation or the adjacent gabbros; or (4) localized and variable assimilation of crust. The samples of the upper gabbro and felsic segregation units are not located near any external contacts (Fig. 2), and field and petrographic observations indicating limited to absent sub-solidus alteration (Figs. 3 and 4) suggest that metasomatism (hypothesis 3 above) and crustal assimilation (hypothesis 4) are not important in driving the isotopic differences. Additionally, neither the gabbro nor the felsic segregation samples plot within the Sr_i seawater-alteration trend (Fig. 6; Hart et al., 1974). All these observations suggest that the observed isotopic differences record magmatic histories.

The higher Yb/Dy and Hf concentrations and lower Ti contents and Eu/Eu* (Fig. 11) in the felsic segregation zircons support the interpretation that the felsic segregation melt was more differentiated than the melt from which the upper gabbro zircons crystallized. Despite both rock types being sampled in close vicinity, the isotopic discrepancy supports the conclusion that the felsic segregation melt was not simply the interstitial melt from the immediately surrounding gabbro. We thus infer that hypotheses 1 and 2 above more likely explain the difference in isotopic composition between the gabbro and the felsic segregation samples: Pre-existing differences in the crystals and melts entering the mush system led to whole-rock isotopic heterogeneity, which was further amplified during late-stage melt extraction from the mush to form felsic segregations. To discriminate between hypotheses 1 and 2, in situ mineral isotopic data should be collected from the major phases. This would also be effective at evaluating the extent (if any) of hydrothermal alteration on Sr isotopes (Tepley and Davidson, 2003).

Several physical mechanisms have been proposed to drive the separation of crystals and melt in a mush at high crystallinity, with compaction involving crystal repacking and/or crystal deformation considered the most efficient (Bachmann and Bergantz, 2006; Holness et al., 2017; Bachmann and Huber, 2019). Elongated plagioclase crystals in the upper gabbro, which define a planar foliation, show deformation twinning and undulose extinction (Figs. 4A–4C), indicating crystal-plastic deformation of a crystal framework during igneous compaction rather than gravitational settling in a melt-rich environment (e.g., Holness, 2018). Field observations also indicate the importance of a fluid phase in the formation of the felsic segregations, which may aid in crystal-melt segregation processes (Sisson and Bacon, 1999): (1) the presence of vesicular textures around many segregations (Figs. 3D and 3E), and (2) large grain sizes in the segregations compared to the gabbros, indicating that fluids likely aided crystal growth. We thus propose that interstitial melts in the gabbros were able to percolate through the crystal mush at high crystallinity and collect to form felsic segregations by a combination of crystal-mush compaction processes and gas-driven filter pressing (e.g., Sisson and Bacon, 1999). The tear shapes of the segregations with rounded to irregular tips indicate that ductile rather than brittle fracturing operated in the crystal mush, which is consistent with the observed visco-plastic behavior of a crystal mush upon intrusion of melt (Bergantz et al., 2015). The structures described here resemble melt segregation pools from granitic plutons described by Weinberg (2006).

5.2.3. Distinct Magma Batches and Crystal Accumulation in the Lower Part of the Complex

The gabbro unit is compositionally and texturally heterogenous, as evident by different modal abundances of olivine, pyroxene, amphibole, and fine-grained and coarse-grained varieties of these minerals (Best, 1963; Putirka et al., 2014; Table 1). For example, field observations in the upper gabbro unit show centimeter- to meter-scale layering of amphibole- and pyroxene-rich layers (Fig. 3B). The lack of a single, well-defined differentiation trend in the whole-rock compositions from the gabbro and meladiorite unit samples (TiO_2,

Al_2O_3, and P_2O_5 versus SiO_2; Putirka et al., 2014, their figure 7) indicates either (1) different degrees of crystal accumulation or melt loss; (2) emplacement of multiple compositionally distinct magma batches; or (3) a combination of both. The previous discussion presented evidence for both processes. Mineral chemistry further supports crystal accumulation processes: Most pyroxene and plagioclase compositions from the gabbro and meladiorite samples are not in equilibrium with their respective host rock compositions (Fig. S2 [see footnote 1]), indicating that whole-rock compositions are too mafic to have been liquid compositions (e.g., Cornet et al., 2022). Mineral chemometers of Higgins et al. (2022) indicate that pyroxene equilibrium melts are andesitic to dacitic (57–68 wt% SiO_2; Table 2) in the lower GIC units, supported by plagioclase chemometers of Scruggs and Putirka (2018) (Table 2). Variation in whole-rock isotope chemistry, on the other hand, provides evidence for the emplacement of individual compositionally distinct magma batches. We thus argue that both mineral accumulation and the emplacement of compositional distinct magma batches occurred. Batch-specific whole-rock isotope signatures could be preserved if most mineral phases crystallized prior to mineral accumulation and melt loss (i.e., adcumulate formation). A rigid mineral framework at these relative high crystallinities would then prevent large-scale mixing between incoming magma batches, but interstitial liquid would still be capable of percolating through a crystal mush to collect in segregations.

5.2.4. An In Situ Differentiation Connection between GIC Units?

The value of $\delta^{18}O_{(melt)}$ can increase during closed-system fractionation due to crystallization of low-$\delta^{18}O$ minerals (e.g., olivine, pyroxene, Fe-Ti oxides; e.g., Bindeman et al., 2004). The extent of this increase depends on the exact differentiation pathway (e.g., crystallization assemblage, temperature, melt SiO_2) and is ≤1‰ during fractionation from basalt to rhyolite (Bindeman et al., 2004; Bucholz et al., 2017). Zircon $\delta^{18}O$ values would vary only by tenths of a per mil due to closed-system fractionation (Bucholz et al., 2017). The variations in $\delta^{18}O_{(WR)}$ and $\delta^{18}O_{(zircon)}$ in all GIC samples (Fig. 8) are larger than can be explained by closed-system fractionation, thus open-system behavior would have been required to explain the observed isotopic compositions.

5.2.5. Pluton-Wide Trends in $\delta^{18}O$: A Combination of Magmatic Processes and High-Temperature Alteration

The low $\delta^{18}O_{(WR)}$ and $\delta^{18}O_{(zircon)}$ values in the gabbro units contrast with higher values observed in the meladiorite and granite units (Fig. 8). Low $\delta^{18}O_{(WR)}$ values in the GIC are similar to $\delta^{18}O_{(WR)}$ values of deformed Mariposa Formation rocks at the base of the GIC (BMFZ; Fig. 8). Textural observations and the presence of melt leucosomes (Fig. 3A) indicate that the BMFZ was active prior, during, and after the emplacement of the GIC under upper amphibolite–facies conditions (Paterson et al., 1987; Vernon et al., 1989). The BMFZ likely provided a pathway for low-$\delta^{18}O$ seawater and/or meteoric waters ($\delta^{18}O_{seawater}$: 0‰; Valley et al., 2005) to reach deeper parts of the crust during the marine Jurassic arc conditions, or seawater could also have been liberated from marine sediments of the Mariposa Formation during deformation (Paterson and Vernon, 2001). High deformation temperatures (>500 °C; Vernon et al., 1989) in the BMFZ would have allowed for water-rock oxygen isotope exchange to produce low-$\delta^{18}O$ rocks in the vicinity of the lowermost units of the GIC. Tobisch et al. (1991) documented low $\delta^{18}O_{(WR)}$ values (~+5‰) in mylonitic Santa Cruz Mountain tonalites (Figs. 1 and 8), interpreted as a result of fluid-enhanced deformation. In addition, a combination of contemporaneous partial melting of previously high-temperature, hydrothermally altered rocks of the Mariposa Formation in the BMFZ and GIC magmatism, as documented by field evidence (Fig. 3A) and zircon U-Pb ages (Fig. 1; Saleeby et al., 1989), would have produced high-silica, low-$\delta^{18}O$ melts (Montel and Vielzeuf, 1997) that could have mixed with the gabbro crystal mush at the base of the GIC. To test such a scenario, we conducted assimilation–fractional crystallization (AFC)–mixing calculations using Sr_i and $\delta^{18}O$ isotopes (Fig. S4; DePaolo, 1981). The composition of a GIC primary magma is unknown but is taken here to be similar to the "western primary magma" for the Sierra Nevada arc from Lackey et al. (2012). We assumed a Mariposa Formation sample as the assimilant with Sr_i of 0.7046 and 184 ppm Sr (Lackey et al., 2012) and $\delta^{18}O_{(WR)}$ of +4.3‰ (lowest value of Mariposa Formation). AFC-mixing calculations show that the low gabbro $\delta^{18}O_{(WR)}$ values can be generated using a ratio of assimilation to fractionation of 0.05–0.4. If the gabbro mush assimilated partial melts from the BMFZ, the amount was likely minor, such that the $\delta^{18}O_{(WR)}$ values in the gabbros did not develop a low-$\delta^{18}O$ magmatic signature (e.g., Troch et al., 2020). However, if the partial melts entered the gabbro mush (potentially through percolation processes) after most Fe-Mg phases had crystallized but before zircon saturation, the $\delta^{18}O_{(zircon)}$ values should record the $\delta^{18}O$ composition of a contaminated melt. The gabbro unit zircon rims show lower $\delta^{18}O_{(zircon)}$ values than their cores (Fig. 9); this might reflect increasing assimilation of low-$\delta^{18}O$ melts during zircon crystallization.

Contrary to the pluton-wide trend of increasing $\delta^{18}O_{(WR)}$ from the exposed base to the top, the uppermost granophyre unit shows lower $\delta^{18}O_{(WR)}$ values than the meladiorite unit below (Fig. 8). The Sr_i values for the granophyres are also distinct from those of the other GIC units: They show a trend toward higher Sr_i at similar ε_{Ndi} (Fig. 6). The relatively low $\delta^{18}O_{(WR)}$ and higher Sr_i values of the granophyres are best explained by high-temperature isotopic exchange with seawater ($\delta^{18}O$: 0‰; $^{87}Sr/^{86}Sr$: 0.7091; Hart et al., 1974; Valley et al., 2005). The widespread granophyric textures (Fig. 4O) attest to large degrees of undercooling at the top of the GIC, i.e., at shallow emplacement levels. The GIC intruded into slightly older marine Mariposa Formation greywacke and slates (Schweickert and Cowan, 1975). Exchange with seawater would have increased the Sr-isotope ratio of altered rocks but have a limited impact on ε_{Nd} (Hart et al., 1974). To acquire the observed low $\delta^{18}O_{(WR)}$ values in the granophyres, alteration must have occurred during elevated temperatures, when isotope mass fractionation is small and altered rocks may approach the low $\delta^{18}O$ values of seawater

(Valley et al., 2005; Troch et al., 2020). Hydrothermal alteration likely took place shortly after solidification, when ambient temperatures were still high (~450 °C) and a hydrothermal system developed at the top of the GIC. This interpretation is supported by the pervasive alteration of the granophyres observed in outcrop (Fig. 3G), thin sections (e.g., sericitization in feldspars, chloritization of mafic minerals), and whole-rock compositions that indicates that some granite and granophyre samples experienced albitization (high Na index; Putirka et al., 2014). Assimilation of Mariposa Formation rocks as an explanation for the high Sr_i and low $\delta^{18}O_{(WR)}$ values in the granophyres is unlikely because the typical Mariposa Formation rocks in the region have high $\delta^{18}O_{(WR)}$ (as high as 13‰; Fig. 8; Lackey et al., 2012) and relative low Sr_i (~0.7046; Lackey et al., 2012). Equally, assimilation of rhyolites at the top of the GIC is also unlikely, given that they have a lower radiogenic Nd isotope composition than the GIC units (Fig. 6).

5.3. Conceptual Model for the GIC: Open-System Processes during Pluton Construction and Subsequent Differentiation and Compositional Modification at Different Scales

In the following, we summarize the main observations and interpretations resulting from this study and place them into a temporal context by combining them with geochronology results from Ratschbacher et al. (2018) and Saleeby et al. (1989) to arrive at a new conceptual model for the GIC:

A. The shallow-marine Mariposa Formation was deposited on top of the Peñon Blanco and Gopher Ridge volcano-clastic formations. Silicic volcanism was active ~2–3 m.y. prior to the onset of GIC construction, as evident by zircon U-Pb crystallization ages of a rhyolitic unit interbedded with the Mariposa Formation (Ratschbacher et al., 2018; Attia et al., 2021; Fig. 12A).

B. Construction of the GIC started with the emplacement of multiple isotopically and chemically distinct mafic to intermediate magma batches at ca. 148.5 Ma, originating from a deeper-seated magma reservoir undergoing differentiation, which formed the lower section of the pluton (Fig. 12B). Distinct compositions are manifested in different mineralogy (e.g., hornblende poor versus hornblende rich) and slightly different $\delta^{18}O_{(WR)}$ and Sr-Nd isotope values. The low $\delta^{18}O_{(WR)}$ and $\delta^{18}O_{(zircon)}$ in GIC gabbros were likely produced through contact with the BMFZ at the base of the GIC, which modified the oxygen isotope composition of the melt by bulk assimilation and/or assimilation of partial melts derived from high-temperature, hydrothermally altered Mariposa Formation rocks (Fig. 12B).

C. Construction continued for ~300 k.y. (Ratschbacher et al., 2018) with the emplacement of felsic magmas in the upper part of the GIC and coeval intrusions of mafic and felsic magmas in the mingling zone (Fig. 12C). The

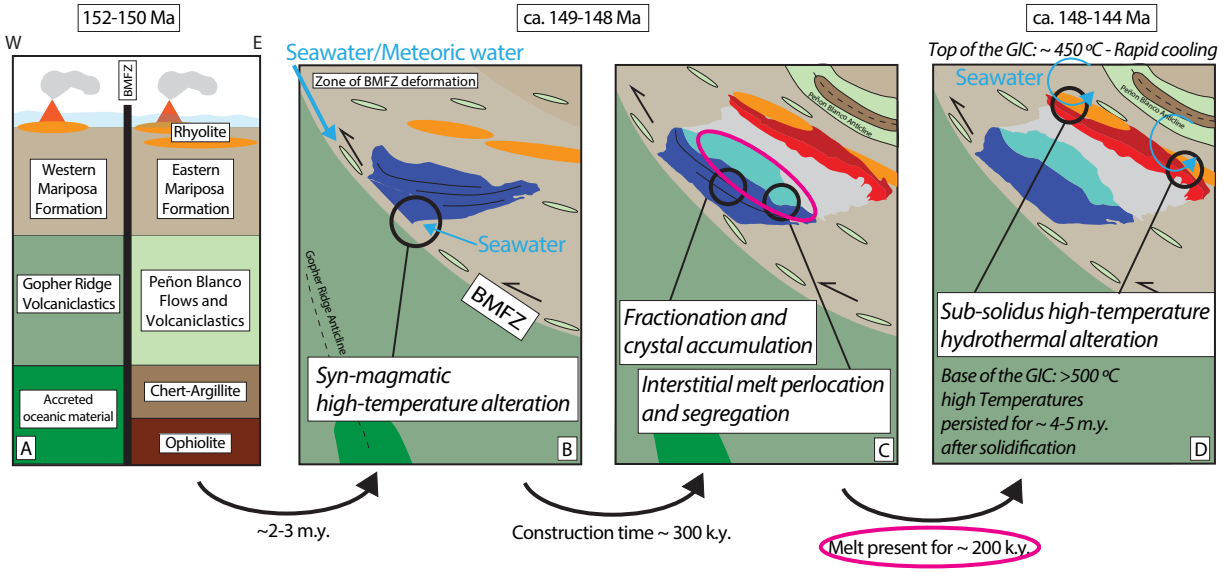

Figure 12. Schematic diagram showing the evolution of the Guadalupe Igneous Complex (GIC) leading to the acquisition of the observed chemical and isotopic characteristics. Letters in each panel follow the steps in the "Conceptual Model" section in text. Panel A shows a schematic cross-section; panels B–D show a map view of the complex. Colors of the GIC are the same as in Figure 2; colors of host rock units are the same as in Figure 1. BMFZ—Bear Mountains fault zone.

range of isotopic values preclude a simple closed-system, in situ differentiation origin for the entire pluton, but open-system differentiation in a crystal mush operated on a smaller scale (e.g., crystal-melt separation). Thermal modeling (Ratschbacher et al., 2018) indicates that melt was present in the central part of the GIC for an extended amount of time (maximum ~500 k.y. including construction and cooling time; pink ellipse in Fig. 12C) from 1000–900 °C liquidus temperatures to ~750–650 °C solidus temperatures (Fig. 5). This facilitated crystal-melt separation and melt migration of chemically and isotopically diverse interstitial melt into felsic segregations and pods (upper gabbro and meladiorite units). The presence of cumulates is also supported by textural observations and pyroxene, amphibole, and plagioclase mineral chemistry.

D. Shortly after solidification, sub-solidus, high-temperature hydrothermal alteration (~450 °C) involving seawater took place at the roof of the complex, affecting $\delta^{18}O_{(WR)}$ and Sr_i values of granite and granophyric rocks (Fig. 12D). At the base of the GIC, high temperatures persisted for 4–5 m.y., as indicated by re-crystallization textures in the lower gabbros (Fig. 4F) and ca. 144 Ma $^{40}Ar/^{39}Ar$ biotite cooling ages from the BMFZ adjacent to the GIC (closure temperatures 300–400 °C). Deformation continued along the BMFZ until ca. 137 Ma.

Integrating zircon U-Pb ages and thermal modeling with $^{40}Ar/^{39}Ar$ cooling ages (Saleeby et al., 1989) and mineral thermometry indicates that (1) the host rocks to the GIC were deposited at least ~2–3 m.y. before magmatism started; (2) construction of the GIC lasted for ~300 k.y., followed by ~200 k.y. of cooling to temperatures of ~750–650 °C; and (3) after solidification, a hydrothermal system developed at the top of the GIC likely caused rapid cooling, whereas the base of the GIC (BMFZ) remained at elevated temperatures (>300–400 °C) for ~4–5 m.y. despite the shallow emplacement level.

6. IMPLICATIONS

This study highlights the benefit of combining different geochemical tools to probe processes at various time (e.g., zircon versus rock-forming mineral chemistry) and length (e.g., detailed transects versus pluton-wide trends) scales to decipher the complex, multi-scale, and open-system magmatic and sub-solidus processes that ultimately result in the integrated chemical and isotopic characteristics of plutonic bodies. In particular, whole-rock data can be misleading if processes, such as crystal accumulation and open-system behavior, operate to modify compositions, which can only be traced by mineral chemistry (e.g., zircon oxygen isotopes and trace elements). However, using mineral chemistry without a context about host magma composition can be misleading because zircon would have crystallized relatively late in mafic samples compared to felsic samples and thus records different stages of melt evolution. This has implications for detrital zircon studies inferring processes such as crustal thickness variations from zircon geochemistry alone (e.g., Tang et al., 2021).

ACKNOWLEDGMENTS

The authors thank Andrew Kylander-Clark at UCSB for help obtaining zircon trace element data, Leslie Hayden at the USGS for help with electron microprobe analyses, and Elizabeth Bell at UCLA for help with secondary ion mass spectrometry (SIMS) analyses. Snir Attia provided a basemap for Figure 1. We also acknowledge the feedback and comments provided by two reviewers and Guest Associate Editor Jonathan Miller that helped to improve the manuscript.

REFERENCES CITED

Annen, C., Blundy, J.D., and Sparks, R.S.J., 2006, The genesis of intermediate and silicic magmas in deep crustal hot zones: Journal of Petrology, v. 47, p. 505–539, https://doi.org/10.1093/petrology/egi084.

Attia, S., Paterson, S.R., Saleeby, J., and Cao, W., 2021, Detrital zircon provenance and depositional links of Mesozoic Sierra Nevada intra-arc strata: Geosphere, v. 17, p. 1422–1453, https://doi.org/10.1130/GES02296.1.

Ayers, J.C., Flanagan, D.M., Miller, C.F., Watson, E.B., and Ryerson, F.J., 2018, Solubility of sphene in siliceous melts: Geological Society of America Abstracts with Programs, v. 50, no. 6, https://doi.org/10.1130/abs/2018AM-320568.

Bachmann, O., and Bergantz, G.W., 2006, Gas percolation in upper-crustal silicic crystal mushes as a mechanism for upward heat advection and rejuvenation of near-solidus magma bodies: Journal of Volcanology and Geothermal Research, v. 149, p. 85–102, https://doi.org/10.1016/j.jvolgeores.2005.06.002.

Bachmann, O., and Huber, C., 2016, Silicic magma reservoirs in the Earth's crust: American Mineralogist, v. 101, p. 2377–2404, https://doi.org/10.2138/am-2016-5675.

Bachmann, O., and Huber, C., 2019, The inner workings of crustal distillation columns: The physical mechanisms and rates controlling phase separation in silicic magma reservoirs: Journal of Petrology, v. 60, p. 3–18, https://doi.org/10.1093/petrology/egy103.

Baertschi, P., 1976, Absolute ^{18}O content of standard mean ocean water: Earth and Planetary Science Letters, v. 31, p. 341–344, https://doi.org/10.1016/0012-821X(76)90115-1.

Barnes, C.G., and Werts, K., 2022, Magma defrosting: Evidence from plutonic rocks: Journal of Petrology, v. 63, https://doi.org/10.1093/petrology/egac112.

Barnes, C.G., Coint, N., and Yoshinobu, A., 2016, Crystal accumulation in a tilted arc batholith: American Mineralogist, v. 101, p. 1719–1734, https://doi.org/10.2138/am-2016-5404.

Barnes, C.G., Werts, K., Memeti, V., and Ardill, K., 2019, Most granitoid rocks are cumulates: Deductions from hornblende compositions and zircon saturation: Journal of Petrology, v. 60, p. 2227–2240, https://doi.org/10.1093/petrology/egaa008.

Barnes, C.G., Coint, N., Barnes, M.A., Chamberlain, K.R., Cottle, J.M., Rämö, O.T., Strickland, A., and Valley, J.W., 2021, Open-system evolution of a crustal-scale magma column, Klamath Mountains, California: Journal of Petrology, v. 62, https://doi.org/10.1093/petrology/egab065.

Barth, A.P., Wooden, J.L., Mueller, P.A., and Economos, R.C., 2016, Granite provenance and intrusion in arcs: Evidence from diverse zircon types in Big Bear Lake Intrusive Suite, USA: Lithos, v. 246–247, p. 261–278, https://doi.org/10.1016/j.lithos.2015.12.009.

Bateman, P.C., 1992, Plutonism in the central part of the Sierra Nevada Batholith, California: U.S. Geological Survey Professional Paper 1483, 186 p., https://doi.org/10.3133/pp1483.

Beard, J.S., 2008, Crystal–melt separation and the development of isotopic heterogeneities in hybrid magmas: Journal of Petrology, v. 49, p. 1027–1041, https://doi.org/10.1093/petrology/egn015.

Bergantz, G.W., Schleicher, J.M., and Burgisser, A., 2015, Open-system dynamics and mixing in magma mushes: Nature Geoscience, v. 8, p. 793–796, https://doi.org/10.1038/ngeo2534.

Best, M.G., 1963, Petrology of the Guadalupe igneous complex south-western Sierra Nevada foothills California: Journal of Petrology, v. 4, p. 223–259, https://doi.org/10.1093/petrology/4.2.223.

Best, M.G., and Mercy, E.L., 1967, Composition and crystallization of mafic minerals in the Guadalupe igneous complex, California: American Mineralogist, v. 52, p. 436–474.

Bindeman, I.N., Ponomareva, V.V., Bailey, J.C., and Valley, J.W., 2004, Volcanic arc of Kamchatka: A province with high-$\delta^{18}O$ magma sources and large-scale $^{18}O/^{16}O$ depletion of the upper crust: Geochimica et Cosmochimica Acta, v. 68, p. 841–865, https://doi.org/10.1016/j.gca.2003.07.009.

Bindeman, I.N., Brooks, C.K., McBirney, A.R., and Taylor, H.P., 2008, The low-$\delta^{18}O$ late-stage ferrodiorite magmas in the Skaergaard intrusion: Result of liquid immiscibility, thermal metamorphism, or meteoric water incorporation into magma?: The Journal of Geology, v. 116, p. 571–586, https://doi.org/10.1086/591992.

Boehlke, J.K., and Kistler, R.W., 1986, Rb-Sr, K-Ar, and stable isotope evidence for the ages and sources of fluid components of gold-bearing quartz veins in the northern Sierra Nevada foothills metamorphic belt, California: Economic Geology, v. 81, p. 296–322, https://doi.org/10.2113/gsecongeo.81.2.296.

Boehnke, P., Watson, E.B., Trail, D., Harrison, T.M., and Schmitt, A.K., 2013, Zircon saturation re-revisited: Chemical Geology, v. 351, p. 324–334, https://doi.org/10.1016/j.chemgeo.2013.05.028.

Bogen, N.L., 1984, Stratigraphy and sedimentary petrology of the Upper Jurassic Mariposa Formation, western Sierra Nevada, California, *in* Crouch, J.K., and Bachman, S.B., eds., Tectonics and Sedimentation along the California Margin: Pacific Section, SEPM (Society for Sedimentary Geology) Book 38, p. 119–134.

Broderick, C., Wotzlaw, J.F., Frick, D.A., Gerdes, A., Ulianov, A., Günther, D., and Schaltegger, U., 2015, Linking the thermal evolution and emplacement history of an upper-crustal pluton to its lower-crustal roots using zircon geochronology and geochemistry (southern Adamello batholith, N. Italy): Contributions to Mineralogy and Petrology, v. 170, 28, https://doi.org/10.1007/s00410-015-1184-x.

Bucholz, C.E., Jagoutz, O., VanTongeren, J.A., Setera, J., and Wang, Z., 2017, Oxygen isotope trajectories of crystallizing melts: Insights from modeling and the plutonic record: Geochimica et Cosmochimica Acta, v. 207, p. 154–184, https://doi.org/10.1016/j.gca.2017.03.027.

Canchola, J., 2016, Geochemical modeling of the Guadalupe Igneous Complex, Mariposa, California [M.S. thesis]: Fresno, California State University, 86 p.

Cashman, K.V., Sparks, R.S.J., and Blundy, J.D., 2017, Vertically extensive and unstable magmatic systems: A unified view of igneous processes: Science, v. 355, https://doi.org/10.1126/science.aag3055.

Claiborne, L.L., Miller, C.F., Walker, B.A., Wooden, J.L., Mazdab, F.K., and Bea, F., 2006, Tracking magmatic processes through Zr/Hf ratios in rocks and Hf and Ti zoning in zircons: An example from the Spirit Mountain batholith, Nevada: Mineralogical Magazine, v. 70, p. 517–543, https://doi.org/10.1180/0026461067050348.

Claiborne, L.L., Miller, C.F., Gualda, G.A.R., Carley, T.L., Covey, A.K., Wooden, J.L., and Fleming, M.A., 2018, Zircon as magma monitor: Robust, temperature-dependent partition coefficients from glass and zircon surface and rim measurements from natural systems, *in* Moser, D.E., Corfu, F., Darling, J.R., Reddy, S.M., and Tait, K., eds., Microstructural Geochronology: Planetary Records Down to Atom Scale: American Geophysical Union Geophysical Monograph 232, p. 1–33, https://doi.org/10.1002/9781119227250.ch1.

Clark, L.D., 1964, Stratigraphy and structure of part of the western Sierra Nevada metamorphic belt, California: U.S. Geological Survey Professional Paper 410, 70 p., https://doi.org/10.3133/pp410.

Clemens-Knott, D.C., 1992, Geologic and isotopic investigations of the early Cretaceous Sierra Nevada batholith, Tulare Co., CA, and the Ivrea Zone, NW Italian Alps: Examples of interaction between mantle-derived magma and continental crust [Ph.D. thesis]: Pasadena, California Institute of Technology, 349 p.

Coint, N., Barnes, C.G., Yoshinobu, A.S., Chamberlain, K.R., and Barnes, M.A., 2013, Batch-wise assembly and zoning of a tilted calc-alkaline batholith: Field relations, timing, and compositional variation: Geosphere, v. 9, p. 1729–1746, https://doi.org/10.1130/GES00930.1.

Connolly, J.A.D., 2005, Computation of phase equilibria by linear programming: A tool for geodynamic modeling and its application to subduction zone decarbonation: Earth and Planetary Science Letters, v. 236, p. 524–541, https://doi.org/10.1016/j.epsl.2005.04.033.

Connolly, J.A.D., 2009, The geodynamic equation of state: What and how: Geochemistry, Geophysics, Geosystems, v. 10, Q10014, https://doi.org/10.1029/2009GC002540.

Cornet, J., Bachmann, O., Ganne, J., Fiedrich, A., Huber, C., Deering, C.D., and Feng, X., 2022, Assessing the effect of melt extraction from mushy reservoirs on compositions of granitoids: From a global database to a single batholith: Geosphere, v. 18, p. 985–999, https://doi.org/10.1130/GES02333.1.

Delph, J.R., Shimizu, K., and Ratschbacher, B.C., 2021, The architecture of the southern Puna magmatic system: Integrating seismic and petrologic observations with geochemical modeling: Journal of Geophysical Research: Solid Earth, v. 126, https://doi.org/10.1029/2020JB021550.

DePaolo, D.J., 1981, A neodymium and strontium isotopic study of the Mesozoic calc-alkaline granitic batholiths of the Sierra Nevada and Peninsular Ranges, California: Journal of Geophysical Research: Solid Earth, v. 86, p. 10,470–10,488, https://doi.org/10.1029/JB086iB11p10470.

Ducea, M.N., Saleeby, J.B., and Bergantz, G., 2015, The architecture, chemistry, and evolution of continental magmatic arcs: Annual Review of Earth and Planetary Sciences, v. 43, p. 299–331, https://doi.org/10.1146/annurev-earth-060614-105049.

Ernst, W.G., Saleeby, J.B., and Snow, C.A., 2009, Guadalupe pluton–Mariposa Formation age relationships in the southern Sierran Foothills: Onset of Mesozoic subduction in northern California?: Journal of Geophysical Research: Solid Earth, v. 114, B11204, https://doi.org/10.1029/2009JB006607.

Ferry, J.M., and Watson, E.B., 2007, New thermodynamic models and revised calibrations for the Ti-in-zircon and Zr-in-rutile thermometers: Contributions to Mineralogy and Petrology, v. 154, p. 429–437, https://doi.org/10.1007/s00410-007-0201-0.

Fiedrich, A.M., Bachmann, O., Ulmer, P., Deering, C.D., Kunze, K., and Leuthold, J., 2017, Mineralogical, geochemical, and textural indicators of crystal accumulation in the Adamello Batholith (Northern Italy): American Mineralogist, v. 102, p. 2467–2483, https://doi.org/10.2138/am-2017-6026.

Fu, B., Page, F.Z., Cavosie, A.J., Fournelle, J., Kita, N.T., Lackey, J.S., Wilde, S.A., and Valley, J.W., 2008, Ti-in-zircon thermometry: Applications and limitations: Contributions to Mineralogy and Petrology, v. 156, p. 197–215, https://doi.org/10.1007/s00410-008-0281-5.

Gevedon, M., 2013, Paired oxygen and hafnium isotopic analysis of zircon from gabbros: Identifying potential Mesozoic mantle heterogeneity in the Sierra Nevada arc [M.S. thesis]: Fullerton, California State University, 77 p.

Gevedon, M.L., and Clemens-Knott, D., 2013, Zircon hafnium and oxygen isotopic analysis of Sierra Nevada gabbros: Evidence for major compositional variations in the Mesozoic mantle: Geological Society of America Abstracts with Programs, v. 45, no. 6, p. 56.

Green, E.C.R., White, R.W., Diener, J.F.A., Powell, R., Holland, T.J.B., and Palin, R.M., 2016, Activity–composition relations for the calculation of partial melting equilibria in metabasic rocks: Journal of Metamorphic Geology, v. 34, p. 845-869, https://doi.org/10.1111/jmg.12211.

Gualda, G.A.R., Ghiorso, M.S., Lemons, R.V., and Carley T.L., 2012, Rhyolite-MELTS: A modified calibration of MELTS optimized for silica-rich, fluid-bearing magmatic systems: Journal of Petrology, v. 53, p. 875–890, https://doi.org/10.1093/petrology/egr080.

Haeussler, P.J., and Paterson, S.R., 1993, Tilting, burial, and uplift of the Guadalupe Igneous Complex, Sierra Nevada, California: Geological Society of America Bulletin, v. 105, p. 1310–1320, https://doi.org/10.1130/0016-7606(1993)105<1310:TBAUOT>2.3.CO;2.

Harper, B.E., Miller, C.F., Koteas, G.C., Cates, N.L., Wiebe, R.A., Lazzareschi, D.S., and Cribb, J.W., 2004, Granites, dynamic magma chamber processes and pluton construction: The Aztec Wash pluton, Eldorado Mountains, Nevada, USA: Earth and Environmental Science Transactions of the Royal Society of Edinburgh, v. 95, p. 277–295, https://doi.org/10.1017/S0263593300001073.

Harrison, T.M., and Watson, E.B., 1984, The behavior of apatite during crustal anatexis: Equilibrium and kinetic considerations: Geochimica et Cosmochimica Acta, v. 48, p. 1467–1477, https://doi.org/10.1016/0016-7037(84)90403-4.

Hart, S.R., Erlank, A.J., and Kable, E.J.D., 1974, Sea floor basalt alteration: Some chemical and Sr isotopic effects: Contributions to Mineralogy and Petrology, v. 44, p. 219–230, https://doi.org/10.1007/BF00413167.

Hayden, L.A., and Watson, E.B., 2007, Rutile saturation in hydrous siliceous melts and its bearing on Ti-thermometry of quartz and zircon: Earth and Planetary Science Letters, v. 258, p. 561–568, https://doi.org/10.1016/j.epsl.2007.04.020.

Hayden, L.A., Watson, E.B., and Wark, D.A., 2008, A thermobarometer for sphene (titanite): Contributions to Mineralogy and Petrology, v. 155, p. 529–540, https://doi.org/10.1007/s00410-007-0256-y.

Higgins, O., Sheldrake, T., and Caricchi, L., 2022, Machine learning thermobarometry and chemometry using amphibole and clinopyroxene: A window into the roots of an arc volcano (Mount Liamuiga, Saint Kitts): Contributions to Mineralogy and Petrology, v. 177, 10, https://doi.org/10.1007/s00410-021-01874-6.

Hildreth, W., 2021, Comparative rhyolite systems: Inferences from vent patterns and eruptive Episodicities: Eastern California and Laguna del Maule: Journal of Geophysical Research: Solid Earth, v. 126, https://doi.org/10.1029/2020JB020879.

Hildreth, W., and Moorbath, S., 1988, Crustal contributions to arc magmatism in the Andes of central Chile: Contributions to Mineralogy and Petrology, v. 98, p. 455–489, https://doi.org/10.1007/BF00372365.

Holland, T.J.B., and Powell, R., 2011, An improved and extended internally consistent thermodynamic dataset for phases of petrological interest, involving a new equation of state for solids: Journal of Metamorphic Geology, v. 29, p. 333–383, https://doi.org/10.1111/j.1525-1314.2010.00923.x.

Holland, T.J.B., Green, E.C.R., and Powell, R., 2018, Melting of peridotites through to granites: A simple thermodynamic model in the system KNCFMASHTOCr: Journal of Petrology, v. 59, p. 881–900, https://doi.org/10.1093/petrology/egy048.

Holness, M.B., 2018, Melt segregation from silicic crystal mushes: A critical appraisal of possible mechanisms and their microstructural record: Contributions to Mineralogy and Petrology, v. 173, 48, https://doi.org/10.1007/s00410-018-1465-2.

Holness, M.B., Vukmanovic, Z., and Mariani, E., 2017, Assessing the role of compaction in the formation of adcumulates: A microstructural perspective: Journal of Petrology, v. 58, p. 643–673, https://doi.org/10.1093/petrology/egx037.

Hoskin, P.W., and Schaltegger, U., 2003, The composition of zircon and igneous and metamorphic petrogenesis: Reviews in Mineralogy and Geochemistry, v. 53, p. 27–62, https://doi.org/10.2113/0530027.

Jennings, E.S., and Holland, T.J., 2015, A simple thermodynamic model for melting of peridotite in the system NCFMASOCr: Journal of Petrology, v. 56, p. 869–892, https://doi.org/10.1093/petrology/egv020.

Keller, C.B., 2021, StatGeochem.jl: Computational tools for statistical geochemistry and petrology: https://doi.org/10.17605/OSF.IO/TJHMW.

Keller, C.B., Schoene, B., Barboni, M., Samperton, K.M., and Husson, J.M., 2015, Volcanic–plutonic parity and the differentiation of the continental crust: Nature, v. 523, p. 301–307, https://doi.org/10.1038/nature14584.

Kistler, R.W., 1990, Two different lithosphere types in the Sierra Nevada, California, *in* Anderson, J.L., ed., The Nature and Origin of Cordilleran Magmatism: Geological Society of America Memoir 174, p. 271–282, https://doi.org/10.1130/MEM174-p271.

Kistler, R.W., and Peterman, Z.E., 1973, Variations in Sr, Rb, K, Na, and initial Sr^{87}/Sr^{86} in Mesozoic granitic rocks and intruded wall rocks in central California: Geological Society of America Bulletin, v. 84, p. 3489–3512, https://doi.org/10.1130/0016-7606(1973)84<3489:VISRKN>2.0.CO;2.

Köhler, T.P., and Brey, G.P., 1990, Calcium exchange between olivine and clinopyroxene calibrated as a geothermobarometer for natural peridotites from 2 to 60 kb with applications: Geochimica et Cosmochimica Acta, v. 54, p. 2375–2388, https://doi.org/10.1016/0016-7037(90)90226-B.

Kylander-Clark, A.R., Hacker, B.R., and Cottle, J.M., 2013, Laser-ablation split-stream ICP petrochronology: Chemical Geology, v. 345, p. 99–112, https://doi.org/10.1016/j.chemgeo.2013.02.019.

Lackey, J.S., Valley, J.W., Chen, J.H., and Stockli, D.F., 2008, Dynamic magma systems, crustal recycling, and alteration in the central Sierra Nevada batholith: The oxygen isotope record: Journal of Petrology, v. 49, p. 1397–1426, https://doi.org/10.1093/petrology/egn030.

Lackey, J.S., Cecil, M.R., Windham, C.J., Frazer, R.E., Bindeman, I.N., and Gehrels, G.E., 2012, The Fine Gold Intrusive Suite: The roles of basement terranes and magma source development in the Early Cretaceous Sierra Nevada batholith: Geosphere, v. 8, p. 292–313, https://doi.org/10.1130/GES00745.1.

Lafrance, B., and Vernon, R.H., 1993, Mass transfer and microfracturing in gabbroic mylonites of the Guadalupe Igneous Complex, California, *in* Boland, J.N., and Fitz Gerald, J.D., eds., Defects and Processes in the Solid State: Geoscience Applications: Amsterdam, Elsevier Science, p. 151–167.

Masi, U., O'Neil, J.R., and Kistler, R.W., 1981, Stable isotope systematics in Mesozoic granites of central and northern California and southwestern Oregon: Contributions to Mineralogy and Petrology, v. 76, p. 116–126, https://doi.org/10.1007/BF00373691.

Miller, R.B., and Paterson, S.R., 1991, Geology and tectonic evolution of the Bear Mountains fault zone, Foothills terrane, central Sierra Nevada, California: Tectonics, v. 10, p. 995–1006, https://doi.org/10.1029/91TC00862.

Montel, J.-M., 1993, A model for monazite/melt equilibrium and application to the generation of granitic magmas: Chemical Geology, v. 110, p. 127–146, https://doi.org/10.1016/0009-2541(93)90250-M.

Montel, J.-M., and Vielzeuf, D., 1997, Partial melting of metagreywackes, Part II. Compositions of minerals and melts: Contributions to Mineralogy and Petrology, v. 128, p. 176–196, https://doi.org/10.1007/s004100050302.

Otamendi, J.E., Ducea, M.N., Tibaldi, A.M., Bergantz, G.W., de la Rosa, J.D., and Vujovich, G.I., 2009, Generation of tonalitic and dioritic magmas by coupled partial melting of gabbroic and metasedimentary rocks within the deep crust of the Famatinian magmatic arc, Argentina: Journal of Petrology, v. 50, p. 841–873, https://doi.org/10.1093/petrology/egp022.

Paterson, S.R., and Vernon, R.H., 2001, Inclusion trail patterns in porphyroblasts from the Foothills Terrane, California: A record of orogenesis or local strain heterogeneity?: Journal of Metamorphic Geology, v. 19, p. 351–372, https://doi.org/10.1046/j.0263-4929.2000.00315.x.

Paterson, S.R., Tobisch, O.T., and Radloff, J.K., 1987, Post-Nevadan deformation along the Bear Mountains fault zone: Implications for the Foothills terrane, central Sierra Nevada, California: Geology, v. 15, p. 513–516, https://doi.org/10.1130/0091-7613(1987)15<513:PDATBM>2.0.CO;2.

Paterson, S.R., Tobisch, O.T., and Vernon, R.H., 1991, Emplacement and deformation of granitoids during volcanic arc construction in the Foothills terrane, central Sierra Nevada, California: Tectonophysics, v. 191, p. 89–110, https://doi.org/10.1016/0040-1951(91)90234-J.

Payacán, I., Gutiérrez, F., Bachmann, O., and Parada, M.Á., 2023, Differentiation of an upper crustal magma reservoir via crystal-melt separation recorded in the San Gabriel pluton, central Chile: Geosphere, v. 19, p. 348–369, https://doi.org/10.1130/GES02535.1.

Putirka, K.D., 2005, Igneous thermometers and barometers based on plagioclase + liquid equilibria: Tests of some existing models and new calibrations: American Mineralogist, v. 90, p. 336–346, https://doi.org/10.2138/am.2005.1449.

Putirka, K.D., 2008, Thermometers and barometers for volcanic systems: Reviews in Mineralogy and Geochemistry, v. 69, p. 61–120, https://doi.org/10.2138/rmg.2008.69.3.

Putirka, K., 2016, Amphibole thermometers and barometers for igneous systems and some implications for eruption mechanisms of felsic magmas at arc volcanoes: American Mineralogist, v. 101, p. 841–858, https://doi.org/10.2138/am-2016-5506.

Putirka, K., Johnson, M., Kinzler, R., Longhi, J., and Walker, D., 1996, Thermobarometry of mafic igneous rocks based on clinopyroxene-liquid equilibria, 0–30 kbar: Contributions to Mineralogy and Petrology, v. 123, p. 92–108, https://doi.org/10.1007/s004100050145.

Putirka, K.D., Mikaelian, H., Ryerson, F., and Shaw, H., 2003, New clinopyroxene-liquid thermobarometers for mafic, evolved, and volatile-bearing lava compositions, with applications to lavas from Tibet and the Snake River Plain, Idaho: American Mineralogist, v. 88, p. 1542–1554, https://doi.org/10.2138/am-2003-1017.

Putirka, K.D., Canchola, J., Rash, J., Smith, O., Torrez, G., Paterson, S.R., and Ducea, M.N., 2014, Pluton assembly and the genesis of granitic magmas: Insights from the GIC pluton in cross section, Sierra Nevada Batholith, California: American Mineralogist, v. 99, p. 1284–1303, https://doi.org/10.2138/am.2014.4564.

Ratschbacher, B.C., Keller, C.B., Schoene, B., Paterson, S.R., Anderson, J.L., Okaya, D., Putirka, K., and Lippoldt, R., 2018, A new workflow to assess emplacement duration and melt residence time of compositionally diverse magmas emplaced in a sub-volcanic reservoir: Journal of Petrology, v. 59, p. 1787–1809, https://doi.org/10.1093/petrology/egy079.

Ridolfi, F., and Renzulli, A., 2012, Calcic amphiboles in calc-alkaline and alkaline magmas: Thermobarometric and chemometric empirical equations valid up to 1,130° C and 2.2 GPa: Contributions to Mineralogy and Petrology, v. 163, p. 877–895, https://doi.org/10.1007/s00410-011-0704-6.

Saleeby, J.B., Geary, E.E., Paterson, S.R., and Tobisch, O.T., 1989, Isotopic systematics of Pb/U (zircon) and $^{40}Ar/^{39}Ar$ (biotite-hornblende) from rocks of the central Foothills terrane, Sierra Nevada, California: Geological Society of America Bulletin, v. 101, p. 1481–1492, https://doi.org/10.1130/0016-7606(1989)101<1481:ISOPUZ>2.3.CO;2.

Saleeby, J.B., Busby-Spera, C., Oldow, J.S., Dunne, G.C., Wright, J.E., Cowan, D.S., Walker, N.W., and Allmendinger, R.W., 1992, Early Mesozoic tectonic evolution of the western U.S. Cordillera, *in* Burchfield, B.C., Lipman, P.W., and Zoback, M.L., eds., The Cordilleran Orogen: Conterminous U.S.: Boulder, Colorado, Geological Society of America, The Geology of North America, v. G-3, https://doi.org/10.1130/DNAG-GNA-G3.107.

Samperton, K.M., Schoene, B., Cottle, J.M., Keller, C.B., Crowley, J.L., and Schmitz, M.D., 2015, Magma emplacement, differentiation and cooling in the middle crust: Integrated zircon geochronological–geochemical constraints from the Bergell Intrusion, Central Alps: Chemical Geology, v. 417, p. 322–340, https://doi.org/10.1016/j.chemgeo.2015.10.024.

Schweickert, R.A., 2015, Jurassic evolution of the Western Sierra Nevada metamorphic province, *in* Anderson, T.H., Didenko, A.N., Johnson, C.L., Khanchuk, A.I., and MacDonald, J.H., Jr., eds., Late Jurassic Margin of Laurasia—A Record of Faulting Accommodating Plate Rotation: Geological Society of America Special Paper 513, p. 299–358, https://doi.org/10.1130/2015.2513(08).

Schweickert, R.A., and Cowan, D.S., 1975, Early Mesozoic tectonic evolution of the western Sierra Nevada, California: Geological Society of America Bulletin, v. 86, p. 1329–1336, https://doi.org/10.1130/0016-7606(1975)86<1329:EMTEOT>2.0.CO;2.

Scruggs, M.A., and Putirka, K.D., 2018, Eruption triggering by partial crystallization of mafic enclaves at Chaos Crags, Lassen Volcanic Center, California: American Mineralogist, v. 103, p. 1575–1590, https://doi.org/10.2138/am-2018-6058.

Sisson, T.W., and Bacon, C.R., 1999, Gas-driven filter pressing in magmas: Geology, v. 27, p. 613–616, https://doi.org/10.1130/0091-7613(1999)027<0613:GDFPIM>2.3.CO;2.

Snow, C.A., and Scherer, H., 2006, Terranes of the western Sierra Nevada Foothills metamorphic belt, California: A critical review: International Geology Review, v. 48, p. 46–62, https://doi.org/10.2747/0020-6814.48.1.46.

Tang, M., Ji, W.-Q., Chu, X., Wu, A., and Chen, C., 2021, Reconstructing crustal thickness evolution from europium anomalies in detrital zircons: Geology, v. 49, p. 76–80, https://doi.org/10.1130/G47745.1.

Tepley, F.J., III, and Davidson, J.P., 2003, Mineral-scale Sr-isotope constraints on magma evolution and chamber dynamics in the Rum layered intrusion, Scotland: Contributions to Mineralogy and Petrology, v. 145, p. 628–641, https://doi.org/10.1007/s00410-003-0481-y.

Tobisch, O.T., Paterson, S.R., Saleeby, J.B., and Geary, E.E., 1989, Nature and timing of deformation in the Foothills terrane, central Sierra Nevada, California: Its bearing on orogenesis: Geological Society of America Bulletin, v. 101, p. 401–413, https://doi.org/10.1130/0016-7606(1989)101<0401:NATODI>2.3.CO;2.

Tobisch, O.T., Barton, M.D., Vernon, R.H., and Paterson, S.R., 1991, Fluid-enhanced deformation: Transformation of granitoids to banded mylonites, western Sierra Nevada, California, and southeastern Australia: Journal of Structural Geology, v. 13, p. 1137–1156, https://doi.org/10.1016/0191-8141(91)90074-S.

Trail, D., Mojzsis, S.J., Harrison, T.M., Schmitt, A.K., Watson, E.B., and Young, E.D., 2007, Constraints on Hadean zircon protoliths from oxygen isotopes, Ti-thermometry, and rare earth elements: Geochemistry, Geophysics, Geosystems, v. 8, Q06014, https://doi.org/10.1029/2006GC001449.

Troch, J., Ellis, B.S., Harris, C., Bachmann, O., and Bindeman, I.N., 2020, Low-$\delta^{18}O$ silicic magmas on Earth: A review: Earth-Science Reviews, v. 208, https://doi.org/10.1016/j.earscirev.2020.103299.

Truschel, J.P., 1996, Petrogenesis of the Fine Gold Intrusive Suite, Sierra Nevada Batholith, California [M.S. thesis]: Northridge, California State University, 137 p.

Valley, J.W., Kinny, P.D., Schulze, D.J., and Spicuzza, M.J., 1998, Zircon megacrysts from kimberlite: Oxygen isotope variability among mantle melts: Contributions to Mineralogy and Petrology, v. 133, p. 1–11, https://doi.org/10.1007/s004100050432.

Valley, J.W., Lackey, J.S., Cavosie, A.J., Clechenko, C.C., Spicuzza, M.J., Basei, M.A.S., Bindeman, I.N., Ferreira, V.P., Sial, A.N., King, E.M., Peck, W.H., Sinha, A.K., and Wei, C.S., 2005, 4.4 billion years of crustal maturation: Oxygen isotope ratios of magmatic zircon: Contributions to Mineralogy and Petrology, v. 150, p. 561–580, https://doi.org/10.1007/s00410-005-0025-8.

Vernon, R.H., and Paterson, S.R., 2001, Axial-surface leucosomes in anatectic migmatites: Tectonophysics, v. 335, p. 183–192, https://doi.org/10.1016/S0040-1951(01)00049-X.

Vernon, R.H., Paterson, S.R., and Geary, E.E., 1989, Evidence for syntectonic intrusion of plutons in the Bear Mountains fault zone, California: Geology, v. 17, p. 723–726, https://doi.org/10.1130/0091-7613(1989)017<0723:EFSIOP>2.3.CO;2.

Webster, J.R., and Wintsch, R.P., 1987, Petrochemistry and origin of the Killingworth dome rocks, Bronson Hill anticlinorium, south-central Connecticut: Geological Society of America Bulletin, v. 98, p. 465–474, https://doi.org/10.1130/0016-7606(1987)98<465:PAOOTK>2.0.CO;2.

Weinberg, R.F., 2006, Melt segregation structures in granitic plutons: Geology, v. 34, p. 305–308, https://doi.org/10.1130/G22406.1.

Werts, K., Barnes, C.G., Memeti, V., Ratschbacher, B., Williams, D., and Paterson, S.R., 2020, Hornblende as a tool for assessing mineral-melt equilibrium and recognition of crystal accumulation: American Mineralogist, v. 105, p. 77–91, https://doi.org/10.2138/am-2020-6972.

White, R.W., Powell, R., and Johnson, T.E., 2014, The effect of Mn on mineral stability in metapelites revisited: New *a–x* relations for manganese-bearing minerals: Journal of Metamorphic Geology, v. 32, p. 809–828, https://doi.org/10.1111/jmg.12095.

Wills, C.J., O'Neal, M.D., Holland, P.J., Parrish, B.M., and Delattre, M.P., 2021, Preliminary geologic map of the east half of the Oakdale 30′ × 60′ quadrangle, California.

Wills, C.J., O'Neal, M.D., Holland, P.J. and Key, E.L., 2022, Preliminary Geologic Map of the Merced 30′× 60′ Quadrangle, California.

Wotzlaw, J.-F., Bindeman, I.N., Schaltegger, U., Brooks, C.K., and Naslund, H.R., 2012, High-resolution insights into episodes of crystallization, hydrothermal alteration and remelting in the Skaergaard intrusive complex: Earth and Planetary Science Letters, v. 355, p. 199–212, https://doi.org/10.1016/j.epsl.2012.08.043.

Zhang, J., Humphreys, M.C.S., Cooper, G.F., Davidson, J.P., and Macpherson, C.G., 2017, Magma mush chemistry at subduction zones, revealed by new melt major element inversion from calcic amphiboles: American Mineralogist, v. 102, p. 1353–1367, https://doi.org/10.2138/am-2017-5928.

Zindler, A., and Hart, S., 1986, Chemical geodynamics: Annual Review of Earth and Planetary Sciences, v. 14, p. 493–571, https://doi.org/10.1146/annurev.ea.14.050186.002425.